frontiers in Earth Science

ORIGINAL RESEARCH
published: 24 September 2019
doi: 10.3389/feart.2019.00239

Deep Magma Storage Revealed by Multi-Method Elemental Mapping of Clinopyroxene Megacrysts at Stromboli Volcano

Teresa Ubide[1]*, *John Caulfield*[1], *Claire Brandt*[1], *Yannick Bussweiler*[2,3], *Silvio Mollo*[4,5], *Flavio Di Stefano*[4], *Manuela Nazzari*[5] and *Piergiorgio Scarlato*[5]

[1] School of Earth and Environmental Sciences, The University of Queensland, Brisbane, QLD, Australia, [2] TOFWERK AG, Thun, Switzerland, [3] Institut für Mineralogie, Universität Münster, Münster, Germany, [4] Department of Earth Sciences, Sapienza - University of Rome, Rome, Italy, [5] Istituto Nazionale di Geofisica e Vulcanologia, Rome, Italy

OPEN ACCESS

Edited by:
Mattia Pistone,
Université de Lausanne, Switzerland

Reviewed by:
Fabio Arzilli,
University of Manchester,
United Kingdom
Chad Deering,
Michigan Technological University,
United States

***Correspondence:**
Teresa Ubide
t.ubide@uq.edu.au

Specialty section:
This article was submitted to Volcanology, a section of the journal Frontiers in Earth Science

Received: 02 March 2019
Accepted: 29 August 2019
Published: 24 September 2019

Citation:
Ubide T, Caulfield J, Brandt C, Bussweiler Y, Mollo S, Di Stefano F, Nazzari M and Scarlato P (2019) Deep Magma Storage Revealed by Multi-Method Elemental Mapping of Clinopyroxene Megacrysts at Stromboli Volcano. Front. Earth Sci. 7:239. doi: 10.3389/feart.2019.00239

The magmatic architecture and physicochemical processes inside volcanoes influence the style and timescale of eruptions. A long-standing challenge in volcanology is to establish the rates and depths of magma storage and the events that trigger eruption. Magma feeder systems are remarkably crystal-rich, and the growth stratigraphy of minerals sampled by erupted magmas can reveal a wealth of information on pre-eruptive processes. Here we combine detailed textural and chemical data acquired on large (>5 mm), euhedral augite megacrysts from Roman era activity (Pizzo scoria cone, 2.4–1.8 ka) at Stromboli (Italy) to investigate the plumbing system prior to the onset of current steady-state activity. Our dataset includes novel laser ablation time-of-flight mass spectrometry (LA-ICP-TOFMS) maps, which rapidly visualise multi-element zoning patterns across entire megacryst sections. The clinopyroxene data are complemented with geochemical constraints on mineral and melt inclusions, and adhering glassy tephra. Megacrysts are sector and oscillatory zoned in trace elements, yet their major element compositions are relatively uniform and in equilibrium with shoshonite-buffered melts. Mild sector zoning documents dynamic crystallisation under conditions of low undercooling during magma residence and growth. Clinopyroxene-melt thermobarometric and hygrometric calibrations, integrated with thermodynamically derived equilibrium equations, accurately track the P-T-H_2O path of magmas. The refined models return restricted crystallisation depths that are deeper than those reported previously for historical and current eruptions, but consistent with deep clinopyroxene-dominated crystallisation (≥10 km), resembling other water-rich alkaline mafic systems. Megacryst cores are overgrown by oscillatory zoned mantles recording continuous input of magma that failed to trigger eruption. Crystal rims are characterised by a mild increase in compatible transition metals Cr and Ni, and depletion in incompatible elements, indicative of pre-eruptive mafic replenishment and magma mixing. The volcanic system appears to have been dominated by protracted periods of replenishment, convection,

and crystal residence, punctuated by rapid megacryst evacuation and eruption upon arrival of more mafic magma (days-weeks). Since the inception of current steady-state activity, eruption-triggering melts have become appreciably more mafic, suggesting that intrusion of primitive magma may be a key driver of the steady-state regime.

Keywords: clinopyroxene, megacryst, sector zoning, oscillatory zoning, elemental mapping, time-of-flight mass spectrometry (ICP-TOFMS), magma mixing, stromboli

INTRODUCTION

The depths and rates of magma storage, transport, mixing, and eruption are of fundamental importance in igneous petrology, and key in the interpretation of monitoring signs at active volcanoes (e.g., McNutt, 2005; White and McCausland, 2016; Biggs and Pritchard, 2017; Cashman et al., 2017). The pathway of mantle-derived magmas through the crust to eruption can be highly convoluted and includes protracted magma segregation, stagnation, and crystallisation in vertically extended mush columns (Cashman et al., 2017), often conspiring against magmas reaching the Earth's surface. As a result, most magmas do not erupt (Putirka, 2017). Indeed, measurements of degassing at active volcanoes infer volumes of shallow magma that greatly exceed erupted volumes (Shinohara, 2008). Understanding the intensive parameters and timescales of the processes that modulate volcano plumbing systems, and identifying those that tip volcanoes to the point of eruption, are key research directions in modern petrology and volcanology (e.g., Putirka, 2017).

Stromboli volcano (Aeolian archipelago, Italy; **Figure 1**) constitutes an ideal natural laboratory for the detailed investigation of magmatic processes and eruption triggers on geological, to historical, to human timescales (e.g., Francalanci et al., 2013). The stratovolcano is an archetype of steady-state activity, where continuous input of basaltic magma has maintained persistent volcanism for centuries, affording the volcano the unique moniker "Lighthouse of the Mediterranean" (Rosi et al., 2013 and references therein). Frequent mild explosions (every 10–20 min) eject crystal-rich black scoriae sourced from a shallow, highly porphyritic (HP) reservoir. The regular "Strombolian" activity is periodically interrupted by more energetic short-lived blasts, "paroxysms," the latest examples of which occurred on July 3rd and August 28th, 2019. Paroxysms typically erupt HP magma mingled with crystal-poor, volatile-rich, more primitive "golden" pumice fed from a deep, low porphyritic (LP) reservoir. More rarely, the volcano produces lava flows, similar in composition to the regular black scoriae and also sourced from the HP reservoir (e.g., Armienti et al., 2007). An improved understanding of the processes controlling the different eruptive styles is a high priority for civil defence (Burton et al., 2007). Syn-eruptive mixing and mush recycling is recorded by chemical and isotopic heterogeneities at the mineral scale, preserved as complex textures in plagioclase and clinopyroxene (e.g., Landi et al., 2004; Francalanci et al., 2005, 2012; Armienti et al., 2007; Bragagni et al., 2014; Petrone et al., 2018). Olivine-hosted melt inclusions locate the current LP-HP double-tier storage system at ca. 10 and 3 km, respectively (Aiuppa et al., 2010; Métrich et al., 2010), within a vertically extended mush column. Precisely locating distinct reservoirs throughout the history of Stromboli volcanism is crucial given the hazard potential of activating magma pockets with distinct crystallinity and volatile contents. However, independent petrological estimates based on mineral-melt equilibrium have been hampered by a lack of calibrations appropriate for Stromboli magmas.

Products erupted during the last two millennia encompass three successive periods of activity (**Figure 1C**): Epoch 6a (Pizzo, San Bartolo, Bastimento, and Post-Pizzo), 6b and 6c (<1.2 ka Present-day activity; Francalanci et al., 2013). In a recent study on the eruptive products of the Post-Pizzo and the Present-day activity, Petrone et al. (2018) concluded that steady-state activity was already established in the Post-Pizzo period. Using bulk rock and clinopyroxene compositions, together with Fe-Mg diffusion modelling of clinopyroxene zoning, Petrone et al. (2018) suggested a link between the arrival of mafic shoshonite magma and the development of a very well-stirred, dynamic plumbing system characterised by rapid mixing and short-storage timescales. The power of mafic intrusions as drivers of enhanced magmatic activity has also been highlighted through clinopyroxene compositions at Mt. Etna (Ubide and Kamber, 2018), a larger stratovolcano situated on the island of Sicily (**Figure 1**) and characterised by annual volcanic activity. At Stromboli, the question remains as to whether the steady-state activity started in Post-Pizzo times or even earlier. Most importantly, there is a need to better understand the key magmatic processes and plumbing system architectures that bring about changes in eruptive activity through time.

Previous products of Roman era volcanism (2.4–1.8 ka; Pizzo activity; **Figure 1**) crop out near the summit of Stromboli and include pyroclastic deposits that can be compositionally divided into two subgroups: shoshonites (similar to Post-Pizzo and Present-day activity eruptive products) and high-K basalts (common in pre-Pizzo activity but not observed subsequently; Francalanci et al., 2013, 2014). Geochemical investigations on the Pizzo deposits are challenging due to strong alteration by acidic fumarolic gases emitted from the active craters (Francalanci et al., 2014 and references therein). However, detailed stratigraphic and geochemical studies reported that the two compositional subgroups, while coeval, were fed by independent reservoirs located at distinct depths (inferred at ∼3 km for the shoshonites and ∼9–11 km for the high-potassium basalts; Francalanci et al., 2014). The lack of interaction between deep and shallow Pizzo reservoirs contrasts with the current LP-HP configuration, suggesting that the plumbing system may

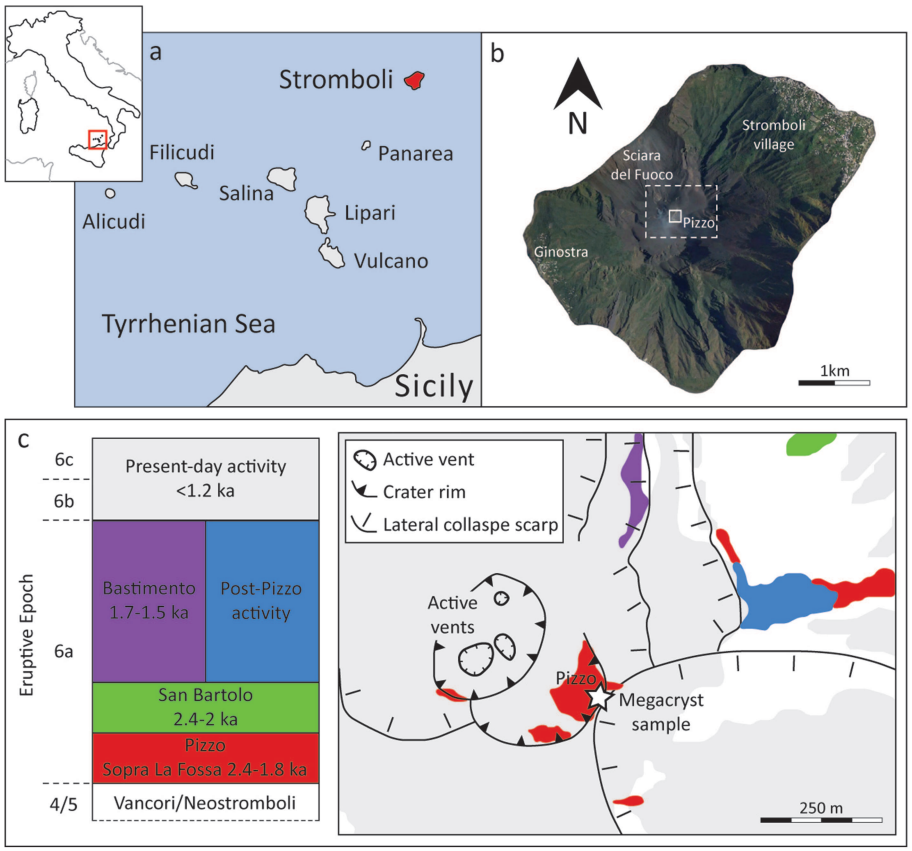

FIGURE 1 | (a) Location of the island of Stromboli in the Aeolian archipelago, Sicily Province, southern Italy. **(b)** Aerial view of Stromboli from Google Earth, outlining summit sample area (Pizzo; solid white square). Dashed white inset denotes location of the geological map in (c). **(c)** Simplified geological map of the Stromboli summit area (modified after Petrone et al., 2018). Legend includes age of eruptive units. The Post-Pizzo activity lacks absolute age constraints but is considered coeval to the Bastimento lavas on the basis of geochemical characteristics (Francalanci et al., 2013). Sampling site is marked with a white star on the map: the clinopyroxene megacrysts were collected from the partially collapsed Pizzo-o-Sopra-la-Fosa (Pizzo) scoria cone, which represents the best viewpoint for observing the Present-day activity at the summit of Stromboli volcano (Francalanci et al., 2014).

have been distinct during Pizzo compared to more recent times. Fresh, perfectly euhedral clinopyroxene (augite) crystals have been long described in these outcrops (Kozu and Washington, 1918) and provide an exciting opportunity to help disentangle protracted magmatic histories and *P-T-*H_2O constraints for a potential turning-point in the eruptive history of Stromboli.

Clinopyroxene is stable over upper mantle and crustal conditions and has low chemical diffusivity, affording the potential to trace eruption triggering mechanisms and timescales in basaltic to intermediate volcanoes (Putirka, 2017; Petrone et al., 2018; Ubide and Kamber, 2018). The composition of clinopyroxene is highly sensitive to pressure, temperature, and melt water content, and recently optimised calibrations on water-rich, mafic alkaline melts (Perinelli et al., 2016; Mollo et al., 2018) open the possibility of new constraints on the architecture of the plumbing system feeding volcanism at Stromboli. Moreover, a recent reappraisal of sector zoning in clinopyroxene (Ubide et al., 2019) has shown that sector-zoned crystals can provide insight not only into magmatic histories and eruption triggers, but also into magma cooling rates and reservoir dynamics. At Stromboli, sector-zoned clinopyroxene has been reported in the products of historical eruptions (Métrich et al., 2010) but to date, the occurrence, record, and implications of sector zoning have remained largely overlooked.

Here we apply a combination of detailed petrography and *in-situ* major and trace element analysis and mapping of clinopyroxene megacrysts (>5 mm) from the Pizzo activity in Roman times, to explore pre-eruptive processes and plumbing system architecture through protracted growth histories. Megacryst sections were prepared parallel and orthogonal to the *c* crystallographic axis to investigate three-dimensional zoning relationships. We applied a multi-method mapping approach combining electron microprobe, laser ablation quadrupole mass spectrometry (Ubide et al., 2015), and novel laser ablation time-of-flight maps (Burger et al., 2015, 2017) for a detailed investigation of zoning patterns, inclusion populations, and their textural context. Petrological results and *P-T-*H_2O estimates of clinopyroxene crystallisation bring new insights into deep

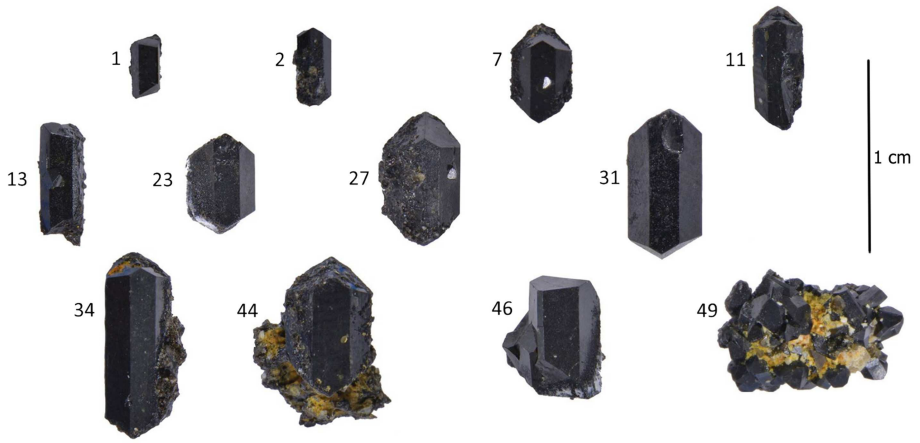

FIGURE 2 | Selection of 12 clinopyroxene megacrysts analysed in this study. The crystals are perfectly euhedral augites, oriented with their *c* crystallographic axis in vertical position (following the scale bar). Crystals 2, 7, 11, 23, 27, 31, 34, and 44 are laying on {100}, whereas 1, 13, and 46 are slightly rotated around the *c*-axis showing {110} in the foreground. Samples 11 and 13 are swallow-tail crystals twinned on {100}. Often, crystals have inclusions of olivine on the surface, remnant inclusion indentations (e.g., 31), and/or are coated with glassy matrix (e.g., 34). Sample 49 is a complex glomerocryst.

magma dynamics and the inception of steady-state activity at Stromboli. Our integrated elemental mapping approach highlights methodological advantages, considerations and limitations, providing guidance for the effective investigation of crystal zoning in magmatic systems elsewhere.

THE CLINOPYROXENE MEGACRYSTS

Clinopyroxene megacrysts were collected at the summit of Stromboli volcano in June 2016, from the remnants of the partially collapsed Pizzo-o-Sopra-la-Fosa (Pizzo) scoria cone (**Figure 1**) which currently forms the best viewpoint for observing the Present-day activity (Francalanci et al., 2014). We collected a single bulk sample that comprises pervasively altered, unconsolidated ash- to lapilli-sized scoria from the top of the Roman-age Pizzo sequence (2.4–1.8 ka; Francalanci et al., 2014, see "psf" in their Figure 2). Loose, perfectly euhedral and fresh clinopyroxene megacrysts (>5 mm), often occurring as glomerocrysts, were readily hand-picked from the weathered scoria. Although the origin of the sample cannot be definitively constrained, the extremely friable nature of the matrix material and presence of loose single megacrysts is consistent with the large crystals having weathered out over the last several thousand years. Megacryst preparation and petrographic observations were undertaken at the School of Earth and Environmental Sciences at The University of Queensland.

Fifty-three megacrysts were carefully cleaned (10–45 min ultrasonication cleaning cycles in 3.5N HCl, milli-Q water, and finally ethanol), weighed, measured, and photographed (**Figure 2**). Crystals were named sequentially based on mass (30–550 mg, clinopyroxene 1 is the lightest) and range from 4 to 17 mm in length. The megacrysts have polyhedral habits following the augite crystal model (e.g., Downes, 1974; Leung, 1974; Ubide et al., 2019), characterised by a consistent set of dominant crystal forms {100}, {110}, {010} perpendicular to the *c*-axis, and {−111} along the *c*-axis (**Figure 3**). Twins on {100} yield swallow-tail crystals elongated along the *c*-axis. Less commonly, twins on {101} form cross-shaped crystals (e.g., Welsch et al., 2016). Non-symmetrical crystal intergrowths are also common. A number of crystals have inclusions of olivine/plagioclase on the surface and/or are partially coated with glassy matrix. Olivine, plagioclase, and matrix glass are variably altered, whereas the clinopyroxenes are invariably fresh.

A subset of 12 representative megacrysts (**Figure 2**; **Supplementary Table 1**) were embedded in resin mounts with their {100} plane face down. Where possible, mounts were then cut in half to expose a cross section perpendicular to the *c*-axis (basal section, named "B"). The two halves were remounted in resin, one parallel and one perpendicular to the *c*-axis, and polished. The section parallel to the *c*-axis (named "C") was polished down to the middle of the crystal with the aim of exposing the entire core-to-rim growth pattern. Reflected light microscopy and back-scattered electron (BSE) imaging guided the selection of crystal sections of interest for *in-situ* analysis and mapping. A summary of crystal sections analysed and techniques applied is provided in **Supplementary Table 1**.

ANALYTICAL METHODS

Major Element Analysis and Mapping Using Electron Microprobe

A total of seven sections from five crystals were analysed for major element compositions by electron probe microanalysis (EPMA) at INGV Rome, using a JEOL JXA-8200 instrument equipped with five wavelength dispersive spectrometers. Analyses were performed on carbon-coated resin mounts under high vacuum conditions, using an accelerating voltage of 15 kV, an electron beam current of 7.5 nA, and a beam diameter of 5 μm. Elemental counting times were 10 s on the peak and 5 s on each

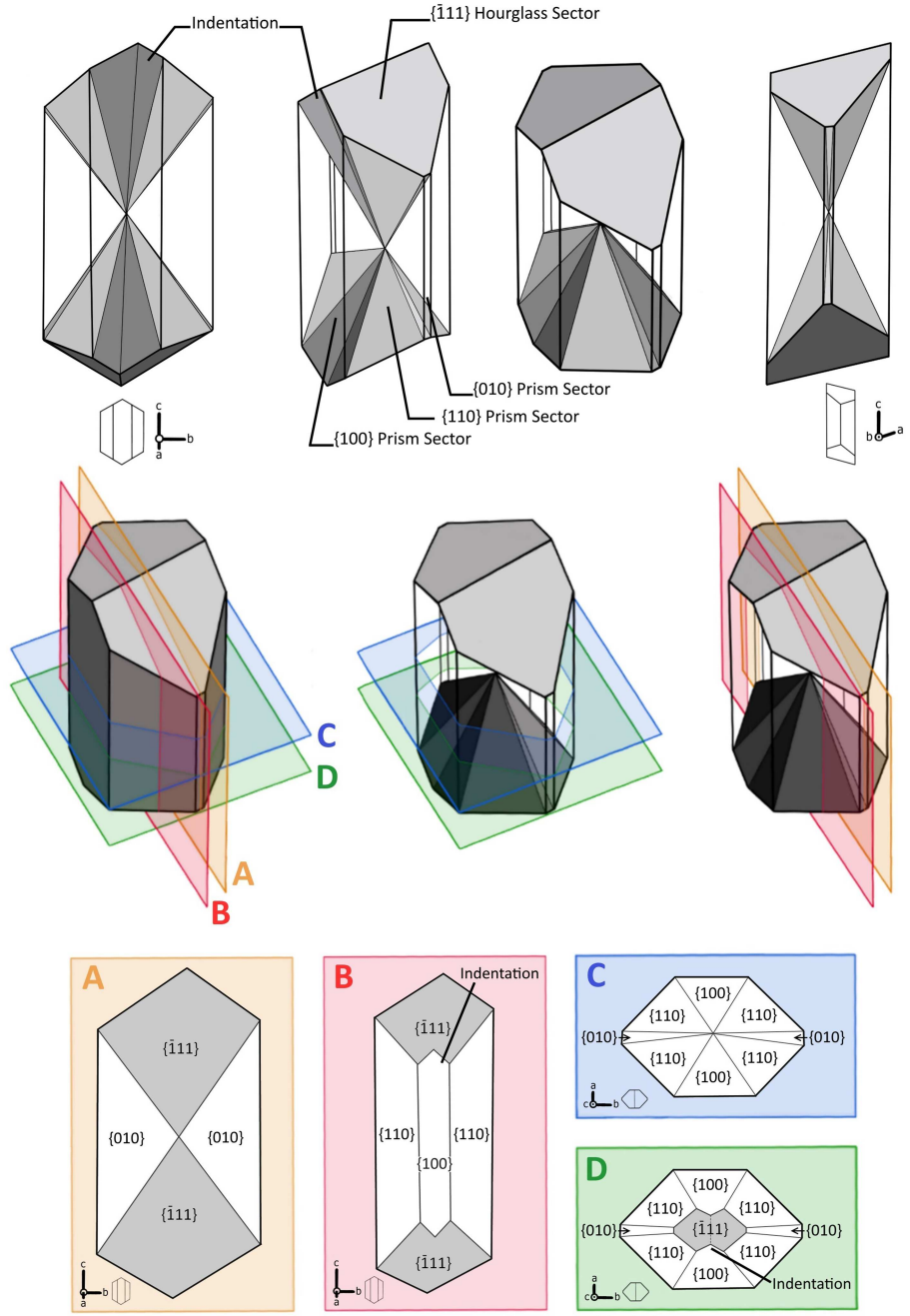

FIGURE 3 | Crystal model based on the habit of sample 31 (**Figure 2**) and following the 12-pyramid morphological model of augite (e.g., Downes, 1974; Leung, 1974; Ubide et al., 2019). The crystal is composed of a total of 12 pyramidal sectors: 8 prism sectors growing perpendicular to the *c*-axis, including the forms {100} x2, {110} x4, and {010} x2, plus 4 hourglass sectors of the form {−111} growing along the *c*-axis. The bottom panel shows theoretical sections along and across the *c*-axis, which expose the prism and hourglass sectors in markedly different locations and shapes. The sections along the *c*-axis are orthogonal to those shown in Ubide et al. (2019): in the present study, elongated sections were prepared along the *c*-*b*-axes, as opposed to the *a*-*c*-axes in Ubide et al. (2019). Note that the angular outline of the hourglass form, generating "valleys" that translate into "indentations" of sector {−111} in two-dimensional crystal sections.

of two background positions. Corrections for inter-elemental effects were made using a ZAF (Z: atomic number; A: absorption; F: fluorescence) procedure. Calibration was performed using a range of standards from Micro-Analysis Consultants (MAC; http://www.macstandards.co.uk): albite (Si-PET, Al-TAP, Na-TAP), forsterite (Mg-TAP), augite (Fe-LIF), apatite (Ca-PET, P-PET), orthoclase (K-PET), rutile (Ti-PET), and rhodonite (Mn-LIF), as well as JEOL Cr metal (Cr-LIF). Rim-to-rim and

TABLE 1 | Instrument parameters used for laser ablation micro-chemical mapping experiments.

		LA-ICP-QMS	LA-ICP-TOFMS
Laser system		**ASI Resolution 193 nm**	**Teledyne Analyte G2 193 nm with ARIS**
Laser parameters	Fluence (J/cm 2)	3	3
	Spot size (μm)	20 × 20	20 × 20
	Stage translation speed (μm/s)	20	200 ("10 pixels per second")
	Repetition rate (Hz)	10	10
	Overlap between rasters in maps (μm)	1	0 (no overlap)
	Background between rasters (s)	20	1–2 (between lines), 20 (before and after entire images)
Gas flows	He (ml/min)	350	600
	Ar (ml/min)	850–920	1,500
	N2 (ml/min)	5	0
Mass spectrometer		**Thermo iCAP RQ**	**iCAP RQ icpTOF (TOFWERK AG)**
ICP-MS parameters	Analytes (dwell times in ms)	7Li (15), 23Na (5), 27Al (5), 43Ca (5)*, 45Sc (10), 51V (10), 52Cr (10), 60Ni (10), 90Zr (10), 139La (15), 146Nd (15)	Entire mass spectrum from 23Na to 238U (30 μs per mass spectrum), 29Si*
	Duty cycle	110 ms	"integration time per pixel" ∼100 ms.
Limits of detection	LODs** (ppm)	7Li (0.2), 23Na (2), 27Al (0.5), 45Sc (0.05), 51V (0.07), 52Cr (1), 60Ni (0.1), 90Zr (0.006), 139La (0.003), 146Nd (0.006)	23Na (120), 27Al (15), 43Ca (1000), 45Sc (3), 51V (1), 52Cr (7), 60Ni (3), 90Zr (0.6), 139La (0.1), 146Nd (0.01)
Mapping times			
Method comparison	Example dimensions (time)	1,632 × 2,088 μm (180 min)	1,632 × 2,088 μm (18 min)

*internal standard. **limits of detection (LODs) calculated following Longerich et al. (1996).

rim-to-core profiles were acquired at 5, 10, or 20 μm step spacing along 1,150–6,300 μm transects. Additional spots targeted mineral and melt inclusions across the megacrysts and in the adhering glassy matrix, where present. Results were screened based on stoichiometry and analytical totals, and the final dataset comprises >3,000 analyses (**Supplementary Tables 2–7**). Smithsonian augite (Jarosewich et al., 1980) and MAC augite were used as quality monitor standards; accuracy and precision were better than 1–5% except for elemental abundances below 1 wt.%, for which accuracy was typically better than 1–10% (n = 20). For EPMA mapping, we used 2.5 × 2.0 to 3.0 × 2.5 μm pixel size and 60 to 90 ms dwell time per pixel, measuring up to five elements per analysis (one per diffracting crystal). Mapped areas varied in size from 2,560 × 2,048 μm to 3,072 × 2,560 μm, with total analytical run times of 19 h 36 min to 29 h 13 min.

Trace Element Mapping Using LA-ICP-QMS

Eleven crystals were investigated using high-resolution laser ablation inductively coupled plasma quadrupole mass spectrometry (LA-ICP-QMS) trace element mapping, following the rastering technique described in Ubide et al. (2015). Most of the crystals were mapped both perpendicular and parallel to the *c*-axis (B and C sections, respectively). Given the large size of the crystals, we selected mapping strips across different crystal faces to reduce analytical run times. In order to effectively resolve elemental zoning in two dimensions across large crystal faces, strips were typically oriented orthogonal to each other.

Mapping experiments were carried out at The University of Queensland Centre for Geoanalytical Mass Spectrometry, Radiogenic Isotope Facility (UQ RIF-lab). We used an ASI RESOlution 193 nm excimer UV ArF laser ablation system with a dual-volume Laurin Technic ablation cell, coupled to a Thermo iCap RQ quadruple mass spectrometer. The laser system was operated with GeoStar Norris software and the mass spectrometer with Qtegra software. Ablation was performed in ultrapure He (grade 5.0, 99.999% purity) to which the Ar make-up gas and a trace amount of N_2 was added for efficient transport and to aid ionisation. Details of laser parameters, gas flows, and mass spectrometer set-up are given in **Table 1**. The instrument was tuned with scans on NIST SRM 612 glass. Elemental maps were built with Iolite (Paton et al., 2011) v2.5 in quantitative mode, using NIST SRM 612 as calibration standard and calcium concentrations in clinopyroxene obtained previously by electron microprobe (21.4 ± 0.3 wt.% CaO; n = 2,924) as internal standard. Accuracy and precision were monitored using BHVO-2G, BCR-2G, BIR-1G, and GSD-1G glass reference materials as quality monitor standards (http://georem.mpch-mainz.gwdg.de/). Accuracy was typically better than 1–10% and precision better than 1–5% (n = 5 for each glass reference material). Limits of detection (Longerich et al., 1996) were at the sub-ppm level for most analysed elements and ≤2 ppm for Na and Cr (**Table 1**).

Multi-Element Mapping Using LA-ICP-TOFMS

Five sections of crystals 31, 34, and 46 were also mapped using laser ablation inductively coupled plasma "time-of-flight" mass spectrometry (LA-ICP-TOFMS) at TOFWERK AG (Thun, Switzerland). We used an icpTOF time-of-flight mass spectrometer (TOFWERK AG, Thun, Switzerland) coupled to an Analyte G2 193 nm excimer laser ablation system (Teledyne CETAC Technologies, Omaha, USA). The laser system was

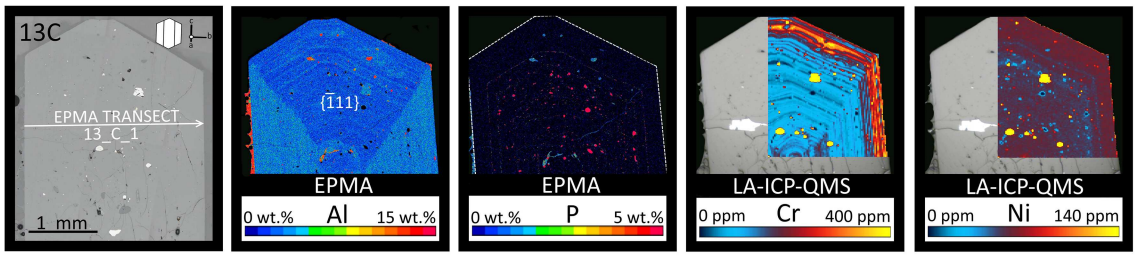

FIGURE 4 | Elongated section of crystal 13, cut along the *c*-axis (section 13C). The section was imaged under reflected light (left panel), and chemically using electron microprobe (Al, P: middle panels) and LA-ICP-QMS (Cr, Ni: right panels). The reflected light image includes a 2D crystal model (top right corner) showing the crystallographic orientation of the section (see also **Figure 3**). Reflected light imaging and micro-chemical mapping provide detailed information on inclusion populations and sector zoning. LA-ICP-QMS maps unveil concentric zonation at the trace element level.

equipped with a HelEx II dual-volume ablation cell and an Aerosol Rapid Introduction System (ARIS) for fast washout of the sample aerosol (Teledyne CETAC Technologies, Omaha, USA). Helium was used as the transport gas, and Ar was added inside the ARIS device prior to introduction of the sample gas into the plasma (see method parameters in **Table 1**). The Analyte G2 laser ablation system was operated with Chromium software (Teledyne CETAC) and the icpTOF mass spectrometer was operated with TOFpilot software (TOFWERK AG). The instrument was tuned with scans on NIST SRM 612 glass. A notch filter was applied to attenuate the Ar peak at 40 m/q.

For analysis of the clinopyroxene samples, "spot-resolved" imaging was performed. This implies that each individual laser shot results in one multi-element pixel in the image (e.g., Burger et al., 2017; Bussweiler et al., 2017). The laser was programmed to raster across the sample area along an array of side-by-side, non-overlapping spots. Based on the signal duration resulting from one laser shot on the sample (measured to be <100 ms), a laser repetition rate of 10 Hz was used. The icpTOF records full mass spectra (from ^{23}Na to ^{238}U) at a rate of 33 kHz (e.g., Borovinskaya et al., 2013), so that multiple measurements are obtained across the signal of a single laser shot. Here, for a single laser-pulse signal with a duration of 100 ms, a total of ∼3,300 mass spectra were acquired and averaged into one pixel. NIST SRM 612 was measured as calibration standard, in the same way as the clinopyroxene images, including gas blanks, immediately before and after each image. Five lines of ∼500 μm length (each lasting 2.5 s) were ablated on the calibration standard during each mapping experiment.

For quantification of the intensity images, the raw data files (HDF5 file format) were processed using an in-house software (Tofware) for TOF baseline subtraction and peak integration (Burger et al., 2017; Hendriks et al., 2017). Images were then quantified against the calibration standard using Iolite software (Paton et al., 2011) with ^{29}Si as the internal standard, assuming a constant content of 23 wt.% Si in clinopyroxene (49.4 ± 0.9 wt.% SiO_2 from microprobe data; n = 2,924). The typical accuracy and precision of the instrument are reported in Burger et al. (2017). Limits of detection for spot-resolved imaging with LA-ICP-TOFMS as employed here were <1 ppm for Zr, La, Nd, <10 ppm for Sc, V, Cr, Ni, ∼10 ppm for Al, and higher for Na (∼120 ppm) and Ca (∼1,000 ppm; **Table 1**). Elemental results from LA-ICP-QMS and LA-ICP-TOFMS methods are comparable in terms of zoning patterns and concentration scales (**Figures 4–6**).

Compositional "Interrogation" of Laser Ablation Maps

Following visual examination of LA-ICP-QMS and LA-ICP-TOFMS zoning maps, we used the Monocle add-on for Iolite (Petrus et al., 2017) to further interrogate the quantified elemental maps and to extract average compositions for individual crystal zones (regions of interest, ROIs). This approach provides high precision concentration data by averaging a large number of data points pooled from compositionally homogeneous ROIs (zones), rather than spatially restricted compositions obtained with classic spot analyses, which are also subject to potential downhole-fractionation (Petrus et al., 2017; Bussweiler et al., 2019). Regions of interest were typically defined using Cr zoning.

RESULTS

Identifying Clinopyroxene Complexity

Under reflected light, the megacryst sections appear remarkably uniform (**Figure 4**), the most notable feature being the abundance of concentrically-distributed mineral and melt inclusions in distinct regions of the crystals (see section Exploring Inclusions Across Megacryst Growth). Electron microprobe major element imaging suggests very mild geochemical variations across the clinopyroxenes (**Figure 4**; **Supplementary Figure 1**). Chemical gradients are almost negligible along concentric zones, and sector zoning is only clear in Al. The hourglass form {−111} is relatively Si-Mg-rich and Al-Ti-Fe-poor compared to prism sectors. However, sectoral variations are minor in Ti and Mg, and very subtle in Si and Fe. Major element maps are best suited as indicators of inclusion populations, the most striking example being apatite (highlighted by EPMA P maps; **Figure 4**).

In contrast, LA-ICP-MS trace element maps reveal marked chemical complexity within the megacrysts (**Figures 4–6**).

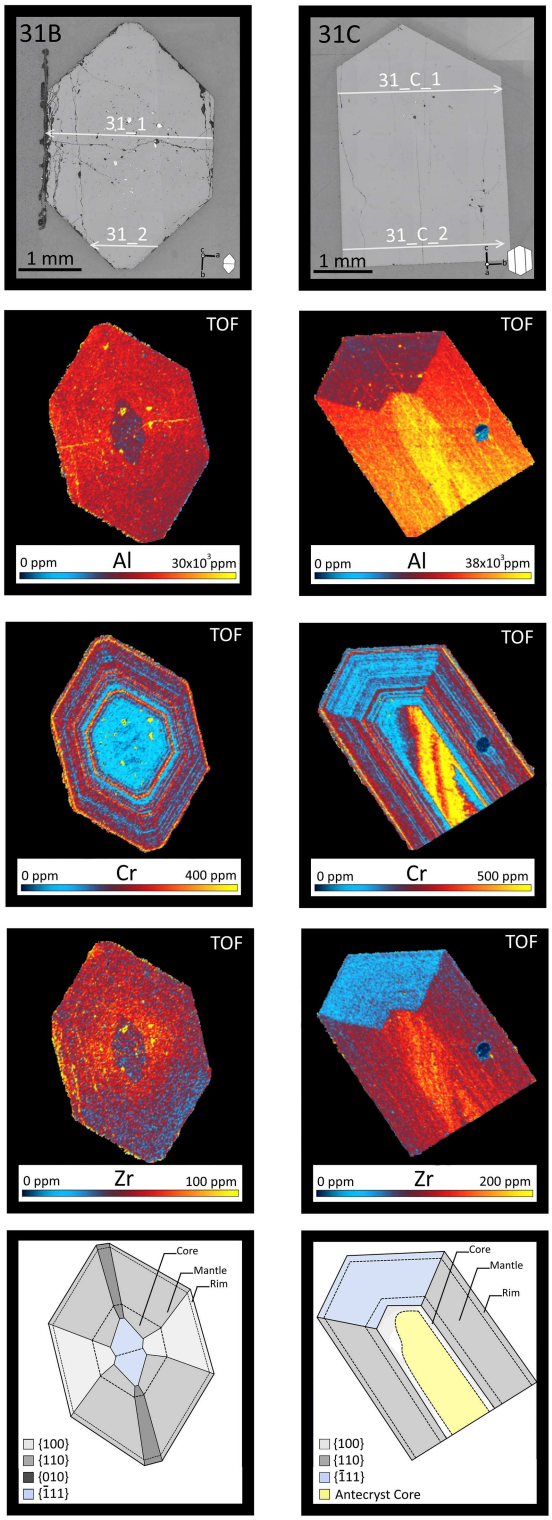

FIGURE 5 | Reflected light scans and LA-ICP-TOFMS maps of crystal 31, cut perpendicular to the *c*-axis (section 31B) and along the *c*-axis (section 31C). This crystal has a perfect polyhedral habit (**Figure 2**) and was used to build the models in **Figure 3**. Chromium shows the largest variations across the crystal, defining a homogeneous, depleted core (~100 ppm), a finely oscillatory zoned *(Continued)*

FIGURE 5 | mantle (140–200 ppm oscillations) and a Cr-rich rim (~280 ppm). The elongate cut 31C contains a recycled antecryst with Cr concentrations up to >400 ppm. The antecryst portion is interpreted to finish shortly after the termination of the crystal cut, as it does not appear in the basal cut 31B. Aluminium contrasts reveal the development of the hourglass {−111} form, occurring in the centre of the basal cut and at the end of the elongate cut (see **Figure 3**). Zirconium follows the zonation in Al. The white arrows on reflected light scans (top) mark the location of EPMA traverses in **Supplementary Figure 3**.

Chromium maps show the sharpest variations, revealing μm-scale oscillations that follow euhedral grain boundaries, producing concentric zonation patterns not reflected in major element compositions (e.g., Mg and Fe). The megacrysts can be subdivided into: homogeneous cores (~90 ppm Cr; $Mg\#_{71-76}$ where Mg# = 100 Mg / (Mg + Fe) with concentrations expressed on a molar basis and Fe = total iron as Fe^{2+}), overgrown by finely oscillatory zoned mantles (70–200 ppm Cr; $Mg\#_{72-78}$), and Cr-rich rims (200–400 ppm Cr; $Mg\#_{72-77}$). Rims show a range of textures from single Cr enrichments (**Figure 5**) to multiple (up to 4) Cr oscillations following euhedral to partially irregular surfaces (**Figures 4**, **6**). Chromium enrichments are mirrored by Ni (80–90 ppm from mantle to rim), along with depletions in mildly incompatible elements, such as La, Nd, and Zr (**Supplementary Figure 2**), suggesting crystallisation from a more mafic melt (Ubide and Kamber, 2018). Some of the crystals contain irregular cores with very high Cr contents (e.g., **Figure 5**; 400–450 ppm Cr), coupled with relative enrichments in Sc, V, and Al, indicative of a recycled (antecryst) origin. Major elements are not significantly different in antecryst cores, with $Mg\#_{73-75}$ variations within the range observed for core, mantle and rim compositions. In addition, cations with high charge including rare earth elements (REE) and high field strength elements (HFSE) show sector zoning following the differential partitioning of Al as a function of crystallographic orientation (**Figures 3**, **4**; **Supplementary Figure 2**; Ubide et al., 2019). Transition metals Cr and Sc show only mild sector zoning, whereas Ni does not partition into sectors (**Figure 4**).

To explore the three-dimensional architecture of zoning patterns, we present LA-ICP-TOFMS maps (TOF maps) of single crystals cut along and perpendicular to the *c*-axis (**Figures 5**, **6**). The TOF-method records a wide range of major and trace element distributions on entire cm-sized sections. The TOF maps corroborate the zonation patterns derived independently using EPMA and LA-ICP-QMS (**Figure 4**) and expand their crystallographic significance, as described below.

Whilst Cr and low charged metals such as Ni and Mn define concentric zonations, Al and highly charged Ti, V, Zr, Hf, and REE (and to a lesser extent Cr and Sc) show clear sector zoning that extends across crystal cores, mantles, and rims (**Figures 3**–**6**). Sector zoning is particularly evident in elongated crystal sections, cut along the *c*-axis (31C and 34C; **Figures 5**, **6**), where the hourglass {−111} form displays sharp indentations following the crystal model depicted in **Figure 3**. Cation depletions in the hourglass {−111} sectors are counterbalanced by enrichments in

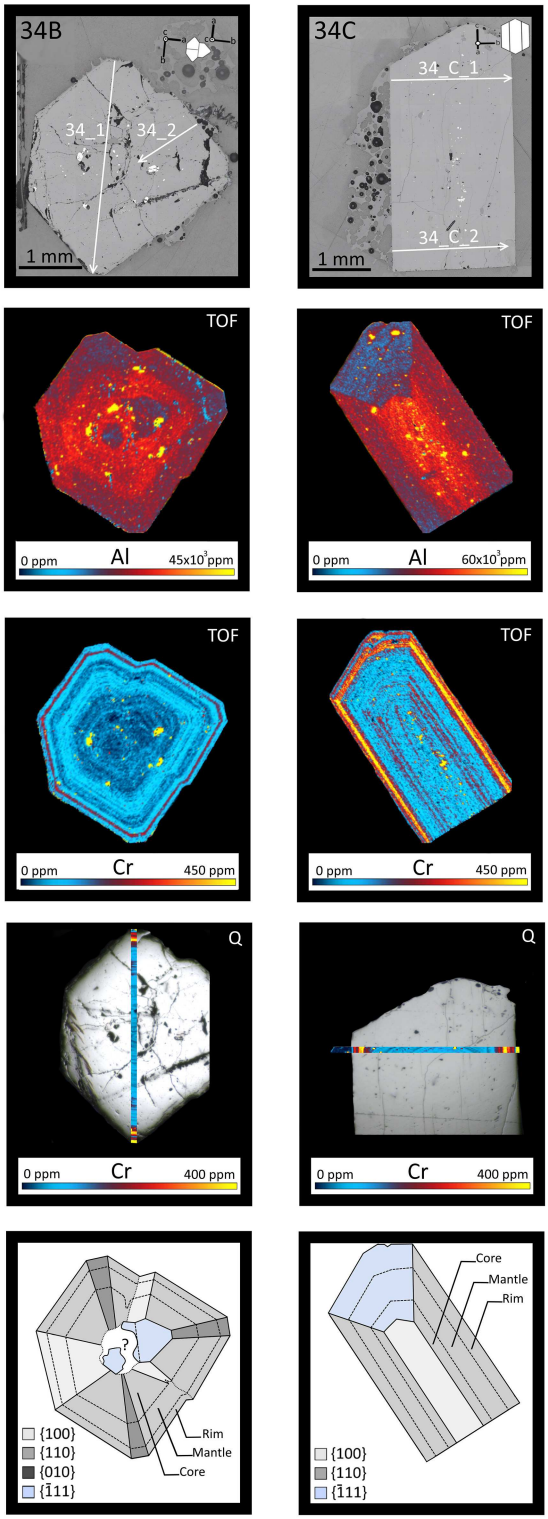

FIGURE 6 | Reflected light scans, LA-ICP-TOFMS and LA-ICP-QMS maps of crystal 34, cut along the *c*-axis (section 34C) and perpendicular to the *c*-axis (section 34B). The basal cut (34B) includes a smaller half-crystal unit oriented parallel to the main crystal but rotated 90-degrees about the *c*-axis. According to Cr zonation, the crystal contains a relatively homogeneous core (~70 ppm Cr) a finely oscillatory zoned mantle (80–110 ppm Cr) and a Cr-rich rim (~260 ppm). The distribution of Al highlights the occurrence of {−111} sectors in both the elongated and basal cuts. The clinopyroxene is partially coated with glassy matrix (shown in the reflected light images at the top), which includes analysed microlites of plagioclase and Ti-magnetite. Note that the TOF-method provides an unparalleled overview of the internal zonation of the crystal, whilst LA-ICP-QMS maps (Q: overlapping strips) targeted specific crystal regions for high-resolution trace element characterisation.

(Continued)

prism sectors {100}, {110}, and {010}. These latter sectors are compositionally almost identical.

The occurrence of compositional contrasts between hourglass and prism sectors in elongated crystal cuts can be extended to basal cuts (31B and 34B; **Figures 5**, **6**), where hourglass sectors are not immediately apparent and can be easily misinterpreted as "inner" cores (**Figure 3**). Indeed, the Cr-poor cores identified in the basal cuts contain what could initially be interpreted as an Al-poor nucleus or "seed" (**Figures 5**, **6**). However, upon closer examination, the Al-poor nuclei display subtle "valleys" that can be linked to the morphological model of the hourglass form (**Figure 3**). The Al-poor zones are, therefore, not inner cores. Rather, they are basal sections of the hourglass {−111} form, characterised by low Al contents (**Figures 5**, **6**). For a given crystal, the mismatch of zoning patterns between the basal cut and the terminated end of the elongate cut is directly related to the re-mounting and re-polishing of the two crystal halves during sample preparation (see section The Clinopyroxene Megacrysts). In crystal 31, re-polishing of the basal section (31B) led to the loss of the antecryst core and exposure of the hourglass form (**Figure 5**).

The stark zoning patterns revealed by multi-element TOF maps, unresolvable using conventional microscopy, provide crystallographic context to test and quantify compositional variations across the megacrysts (e.g., **Figures 5**, **6**, bottom panels). We use the mapping results to locate and classify individual microprobe analyses into sectors ({−111}, {100}, {110}, {010}) as well as concentric zones (antecryst core, regular core, mantle, rim). Traverses across megacryst 31 (**Figures 2**, **3**, **5**) are presented in **Supplementary Figure 3** and illustrate the minimal extent of major element variations across concentric zones. The traverses highlight the contrast between hourglass and prism sectors (**Supplementary Figure 3**); however, this compositional change would likely remain unnoticed or misinterpreted without the elemental maps for context. Additional transects across the studied crystals (e.g., **Figures 4**, **6**) form a large major element dataset that is graphically summarised in **Figure 7**. As observed in electron microprobe maps (**Figure 4**; **Supplementary Figure 1**), major elements are unzoned relative to core, mantle, and rim regions, and sectoral partitioning is only resolvable for hourglass vs. prism sectors (**Figure 7**; **Supplementary Figure 3**). The hourglass sectors {−111} plot in distinct compositional regions with shifts of up to +3 wt.% SiO_2, +1.5 wt.% MgO, −2 wt.% Al_2O_3, −0.5 wt.% TiO_2 and −1 wt.% FeO^T (total iron as FeO) compared to prism sectors (**Figure 7**). The prism sectors ({100}, {110}, and {010}) are compositionally indistinguishable within analytical uncertainty. All sectors have

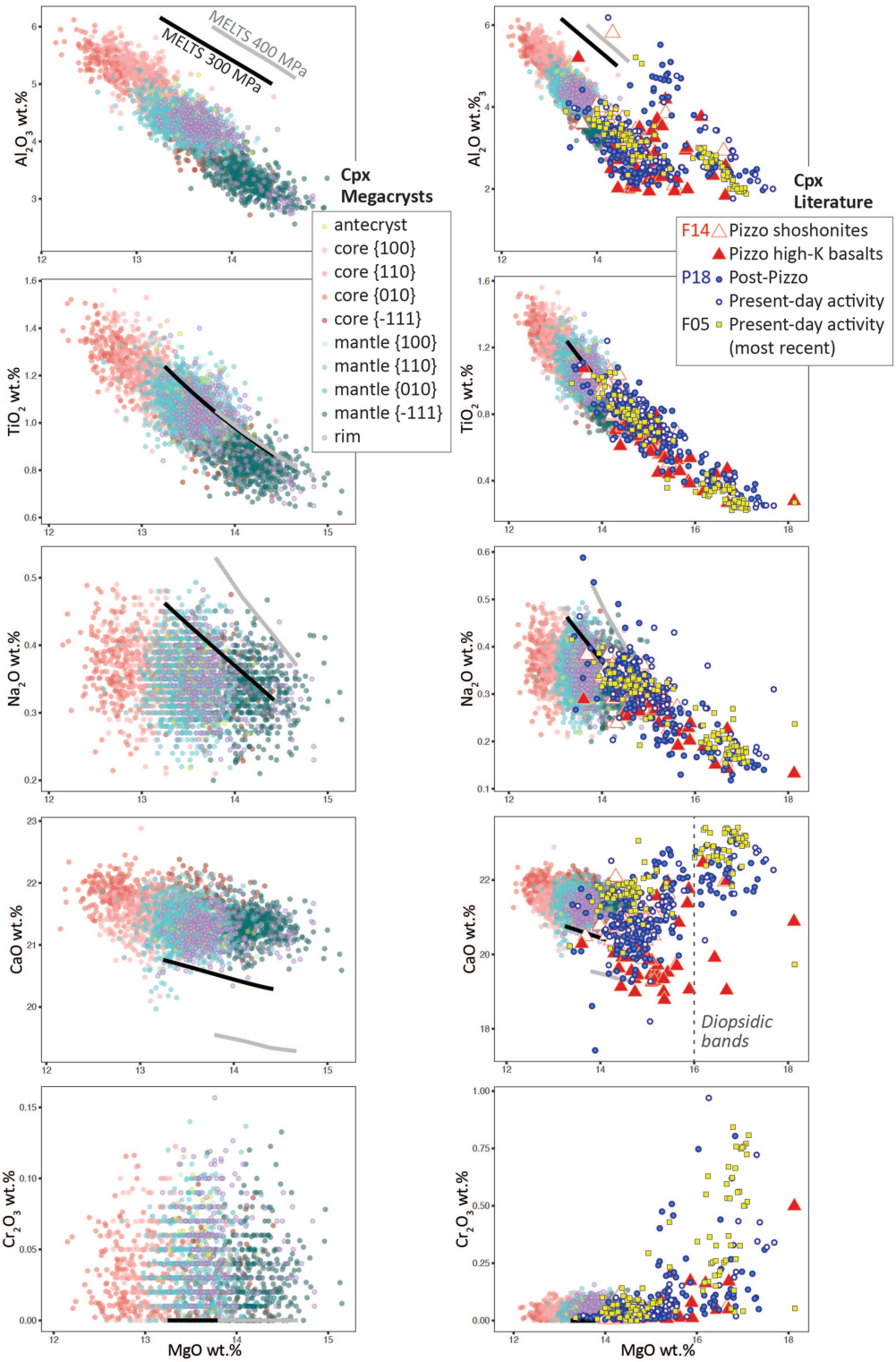

FIGURE 7 | Clinopyroxene compositional variations. **(Left)** Major element compositions across the clinopyroxene megacrysts, obtained by electron microprobe. The data from core, mantle and rim regions are largely coincident, however crystal cores reach highest Al_2O_3-Ti_2O and lowest Si_2O-MgO concentrations. Note the overlap among prism sectors {100}, {110}, and {010}, and the MgO-rich and Al_2O_3-poor composition of hourglass sectors {−111} compared to prism sectors. The black and gray lines represent the evolution of fractionated clinopyroxene modelled with Rhyolite-MELTS (Gualda et al., 2012) from 1,090°C (high MgO) to 1,030°C (low MgO) at isobaric conditions of 300 and 400 MPa, respectively; Rhyolite-MELTS fractionation at 300 MPa reproduces the mineral assemblage and the overall

(Continued)

FIGURE 7 | compositional characteristics of the megacrysts, and is in agreement with thermobarometric and hygrometric results (**Figure 8**). **(Right)** Comparison of megacryst compositions (same data and symbols as in the left panel) with previous data from Pizzo clinopyroxene (F14: Francalanci et al., 2014; shoshonites and high-K products), as well as Post-Pizzo and Present-day clinopyroxene (P18: Petrone et al., 2018), including recent crystals from 1984 to 1996 eruptions (F05: Francalanci et al., 2005). Note that Pizzo shoshonite clinopyroxenes are similar to mantle and rim compositions in the megacrysts. From the Pizzo high-K subgroup through Post-Pizzo to Present-day activity (for stratigraphic context see **Figure 1**), clinopyroxenes contain diopsidic bands relatively enriched in MgO-CaO-Cr_2O_3.

similar concentrations of CaO and Na_2O. Chromium variations are not resolvable, being below the detection limit of EPMA, even for recycled antecrysts. Compared to clinopyroxene phenocrysts from Mt. Etna (Sicily, Italy; Ubide et al., 2019), sector zoning in Stromboli megacrysts is very weakly developed (**Figure 7**), but the relative partitioning of elements between hourglass and prism sectors is similar. Building on constraints from cooling experiments (Mollo et al., 2010, 2013) and natural samples from alkaline systems (Mollo et al., 2011, 2015; Scarlato et al., 2014; Ubide et al., 2014; Gernon et al., 2016; Ubide and Kamber, 2018), we checked for the occurrence of Al_2O_3-TiO_2 enrichments in the outermost growth layers of the crystals. Increased uptake of these incompatible cations within the crystal structure could be related to kinetically-controlled crystal growth caused by high rates of undercooling during rapid magma ascent and eruption. However, we did not find resolvable Al-Ti-rich outer rims for the studied megacrysts, suggesting that crystallisation occurred at depth and possibly under conditions of near-equilibrium cation partitioning.

Our data are similar to smaller clinopyroxenes (phenocrysts and microcrysts) hosted in the regular shoshonite basalts from the Pizzo sequence at Stromboli (**Figure 7**, right panels; Francalanci et al., 2014). In detail, the smaller crystals mirror the compositions of megacryst mantles ad rims, whereas megacryst cores are slightly more evolved (MgO-poor). In contrast with shoshonite crystals, the high-K clinopyroxenes from Pizzo reach higher MgO values. Compared to clinopyroxene compositions from more recent eruptions (Post-Pizzo and Present-day activity, i.e., Epochs 6a-late and 6c; Francalanci et al., 2005; Petrone et al., 2018), the megacrysts (Pizzo, i.e., Epoch 6a-early) have remarkably low MgO, CaO, and Cr_2O_3 concentrations (**Figure 7**, right panels). Essentially, the megacrysts lack the "diopsidic bands" of clinopyroxenes from recent eruptions, recognised optically as concentric zones of lighter colour under plane polarised light and darker grayscale contrast in BSE images (Francalanci et al., 2004, 2005; Landi et al., 2006; Petrone et al., 2018). The implications of these observations will be discussed later.

Exploring Inclusions Across Megacryst Growth

The megacrysts are speckled with μm-sized inclusions of varied compositions (**Figures 4–6**). In major element maps, melt inclusions have irregular outlines enriched in Al and Na relative to their host. Inclusions of plagioclase, titanomagnetite and olivine are relatively rounded and define "hotspots" of Si-Al, Ti-Fe, and Mg-Mn, respectively. Apatite crystals are readily distinguished as P-Ca enrichments, and show equant to tabular shapes depending on sectioning angle. Trace element maps highlight the compositional contrasts expected for each inclusion type (e.g., Ni-rich inclusions are olivine; REE-rich inclusions are apatite). In addition, some of the megacrysts have patches of glassy groundmass attached to their outer surface (**Figure 4**, see Al map; **Figure 6**, see reflected light images), providing textural and compositional information on the final erupted melt. The groundmass glasses are compositionally similar to melt inclusions in the megacrysts (**Supplementary Figure 4**), whilst the chemistry of groundmass microcrysts (typically plagioclase) agrees with that of mineral inclusions.

Importantly, EPMA analyses indicate that the melt feeding crystal growth was chemically homogeneous, maintaining a shoshonitic composition across the entire growth history of the megacrysts (**Supplementary Table 7**). On average, melt inclusions and groundmass glasses return major element concentrations (52.4 ± 0.5 wt.% SiO_2, 3.5 ± 0.2 wt.% MgO, 4.7 ± 0.3 wt.% K_2O, normalised on a 100 wt.% anhydrous basis; $n = 70$) comparable to those of glasses analysed in the Pizzo-shoshonite series (Francalanci et al., 2014) and the Present-day activity (Petrone et al., 2018; **Supplementary Figure 4**). These studies showed that glass compositions are more evolved than whole rocks, which have similar SiO_2 concentrations but higher MgO (4.5–7.0 wt.%; anhydrous basis) and lower K_2O (1.5–3.0 wt.%; anhydrous basis; Francalanci et al., 2014; Petrone et al., 2018). We note that the Pizzo products are strongly porphyritic, and the shoshonite subgroup typically contains 30–45 vol.% of plagioclase, clinopyroxene and less commonly olivine phenocrysts (Francalanci et al., 2014). Consequently, bulk rock compositions constitute mixtures of crystals and melt that may not be representative of true liquids (crystal-free melts; e.g., Francalanci et al., 2004; Reubi and Blundy, 2007; Cashman and Blundy, 2013; Ubide et al., 2014). The constancy of melt inclusion and groundmass glass compositions during the entire growth of megacryst sections reflects the buffering effect of magma recharge episodes on the erupted magma compositions (e.g., Landi et al., 2004, 2008), as described for the mafic alkaline products at Mt. Etna volcano (Peccerillo, 2005; Armienti et al., 2013).

Most mineral inclusions are homogeneously distributed across the megacrysts and show restricted compositional variations. Plagioclase inclusions and microcrysts show $An_{70\pm5}$ ($n = 62$; **Supplementary Table 4**). Olivine inclusions are less common but are compositionally homogeneous at Fo_{72} ($n = 10$; **Supplementary Table 3**). Titanomagnetite inclusions and one analysed titanomagnetite microcryst are also relatively consistent in composition (9.6 ± 0.6 wt.% TiO_2; $n = 50$; **Supplementary Table 5**) except for Cr_2O_3, which is generally at 0.2–0.3 wt.% concentration levels but increases up to 0.5–0.6 wt.% in inclusions hosted in Cr-rich clinopyroxene rims.

In contrast to other mineral inclusions, apatites are oriented along concentric growth bands and occur within the core

and mantle of the megacrysts, but are not found at rims or groundmass (**Figure 4**), nor within recycled antecryst cores. The link between apatite occurrence and concentric zoning in clinopyroxene suggests changes in apatite saturation conditions throughout the megacryst growth history. Apatite compositions are constant across the database (52.8 ± 0.5 wt.% CaO, 43.2 ± 0.5 wt.% P_2O_5; $n = 40$; **Supplementary Table 6**). Halogen concentrations were not determined for this study.

Estimating Clinopyroxene Crystallization Conditions (*P-T*-H_2O)

To investigate the temperature, depth, and water content of the melt from which the megacrysts grew, we combined the major element dataset on clinopyroxene with a representative melt composition to apply thermobarometric and hygrometric calibrations. The melts sampled throughout the entire clinopyroxene history are homogeneous and relatively evolved, as documented by EPMA analysis of melt inclusions and groundmass glasses (**Supplementary Figure 4**). We chose a relatively primitive matrix glass composition within the dataset, with 52.4 wt.% SiO_2, 15.2 wt.% Al_2O_3, 3.6 wt.% MgO, and 10.0 wt.% FeO^T (anhydrous basis; see complete composition in **Supplementary Table 7**, analysis 34_A3_glass5).

A plethora of clinopyroxene-melt equilibrium models based on experimental and thermodynamic data attest to the achievement of near-equilibrium conditions between all clinopyroxene compositions and the selected melt (**Supplementary Figure 5**). One of the most widely used tests for equilibrium is the Fe-Mg exchange coefficient $K_D(\text{Fe-Mg})^{cpx-melt}$, with an equilibrium range refined at 0.28 ± 0.08 by Putirka (2008). Whilst our data return equilibrium Fe-Mg conditions (**Supplementary Figure 5**), the $K_D(\text{Fe-Mg})^{cpx-melt}$ coefficient is known to be dependent on temperature and melt composition (Putirka, 2008; Villaseca et al., 2019), and does not respond to potential kinetic effects during crystal growth (Mollo et al., 2013; Mollo and Hammer, 2017). In fact, the value of 0.28 ± 0.08 represents the weighted arithmetic mean of a much broader equilibrium range of 0.04–0.68 obtained by regressing clinopyroxene-melt compositions from phase equilibrium experiments (Putirka, 2008). Therefore, we applied additional, more robust equilibrium tests that rely on the difference between measured vs. predicted diopside + hedenbergite components ($\Delta DiHd$ of Putirka et al., 1996; Mollo et al., 2013) and clinopyroxene-melt partition coefficients between clinopyroxene and melt (D_{Na} and D_{Ti} of Blundy et al., 1995; Hill et al., 2011, respectively) (cf. details on clinopyroxene-melt equilibrium tests in Mollo et al., 2018; Ubide et al., 2019). The agreement between measured and predicted values for all mineral-melt tests (**Supplementary Figure 5**) supports the reliability of clinopyroxene-melt *P-T*-H_2O estimates for the clinopyroxene compositional database presented here.

We adopted the clinopyroxene-melt barometric, thermometric and hygrometric equations recently optimised by Mollo et al. (2018) for alkaline melts: *P*-independent thermometer 33_{MAM} (±28°C uncertainty), *T*-dependent barometer A_{MAM} (±150 MPa uncertainty) and *P-T*-dependent hygrometer H_{MAM} (±0.5 wt.% H_2O uncertainty). The new calibrations are based on the equations of Putirka et al. (2003) and Perinelli et al. (2016) for *P-T* and H_2O, respectively, and refined for a large dataset of clinopyroxene-melt pairs from alkaline, oxidised and water-rich magmas at Mt. Etna volcano. Stromboli magmas are shoshonitic and highly oxidised (Métrich and Clocchiatti, 1996) and our (relatively evolved) melt returns low clinopyroxene saturation temperatures of 1,080–1,098°C (modelled with the melt-only thermometric equation 34 of Putirka, 2008; ±45°C uncertainty), well within the calibration range indicated by Mollo et al. (2018).

Initial results for crystallisation pressures, temperatures, and melt water contents determined for clinopyroxene megacrysts were 322 (±33) MPa, 1,054 (±7)°C, and 1.8 (±0.2) wt.% H_2O, respectively, where numbers in brackets refer to the standard deviation. The remarkable homogeneity of clinopyroxene major element compositions (**Figures 4–7**) translates into almost constant *P-T*-H_2O results across core, mantle and rim regions, as well as across hourglass and prism sectors. Indeed, the standard deviation values on $n = 2{,}924$ estimates are within error of the barometric, thermometric, and hygrometric models, indicating very stable conditions of crystallisation. To determine the most likely *P-T*-H_2O conditions, we adjusted the *P-T* estimates within the calibration errors of the barometer (±150 MPa) and thermometer (±28°C) to minimise the value of $\Delta DiHd$, thus approaching the ideal equilibrium condition of $\Delta DiHd = 0$ (cf. Mollo and Masotta, 2014). The equilibrium correction provided the most reliable crystallisation conditions for the megacrysts: 1,082 ± 7°C (+28°C addition to T estimates), 316 ± 33 MPa (−6 MPa subtraction from P estimates), and 2.0 ± 0.2 wt.% H_2O (+0.2 wt.% addition to H_2O estimates; **Figure 8**). It is worth noting that water contents are not directly modulated by $\Delta DiHd$, but follow *P-T* adjustments. Interestingly, the corrected temperature data approach the saturation temperature of clinopyroxene in the melt (1,080–1,098°C according to equation 34 of Putirka, 2008 as outlined above) and fall within the range of temperatures obtained for compositionally similar clinopyroxenes in Post-Pizzo and Present-day activity products (1,040–1,089°C; low-Mg# zones in Petrone et al., 2018) using clinopyroxene-melt thermometry (Putirka, 2008).

To provide further constraints on the intensive variables controlling the crystallisation conditions of the Stromboli megacrysts, we conducted thermodynamic simulations using Rhyolite-MELTS software v1.2.0 (Gualda et al., 2012). The applicability of this established algorithm to potassic and "exotic" magma compositions typical of many volcanic settings in Italy has been documented by several authors, as in the case of the Campi Flegrei Volcanic Fields (Fowler et al., 2007) and the Sabatini Volcanic District (Del Bello et al., 2014). The fractional crystallisation path of the melt in equilibrium with clinopyroxene megacrysts was modelled at 1,250–1,000°C, 2 wt.% H_2O and fO_2 buffered at nickel–nickel oxide (NNO; Métrich and Clocchiatti, 1996; Di Carlo et al., 2006) and results are presented in **Supplementary Table 8**. At 400 MPa isobaric conditions, the thermodynamic data reproduced the mineral assemblage observed in the megacrysts. Spinel (titanomagnetite) is the liquidus phase (1,250°C), followed by apatite (1,130°C),

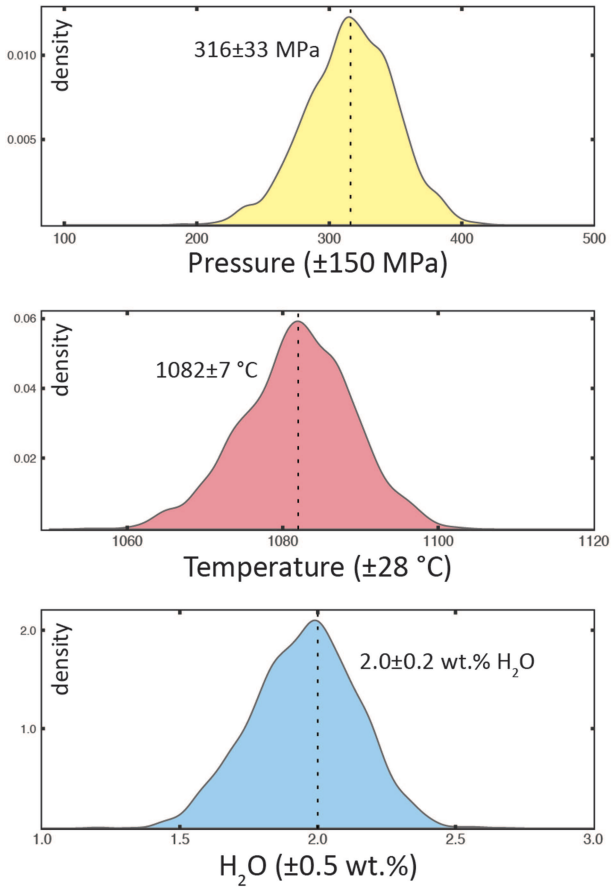

FIGURE 8 | Kernel Density Estimates (KDEs) of magmatic pressure, temperature, and melt water content according to the integrated clinopyroxene-melt calibrations by Mollo et al. (2018), optimised for alkaline basaltic compositions from Mt Etna and further adjusted to minimise deviations from Cpx-melt equilibrium [see details in section Estimating Clinopyroxene Crystallisation Conditions (*P-T*-H2O)]. Dashed dotted lines and figures represent mean and standard deviation values for *P-T*-H_2O estimates: 316 ± 33 MPa, 1,082 ± 7°C, and 2.0 ± 0.2 wt.% H_2O ($n = 2{,}924$). The constancy of thermobarometric and hygrometric results (within error of the calibrations: A_{MAM} ± 150 MPa, 33_{MAM} ± 28°C, H_{MAM} ± 0.5 wt.% H_2O) indicate very stable conditions throughout the crystallisation of the megacrysts. Clinopyroxene-melt equilibrium tests are presented in **Supplementary Figure 5**.

olivine (1,110°C), and finally clinopyroxene (1,090°C), which drives the majority of solid fractionation from the liquid (of the total fractionated assemblage, 47.5% mass is clinopyroxene). The composition of clinopyroxene, however, matches our megacryst compositions more accurately at 300 MPa than at 400 MPa (see isobaric fractionation patterns in **Figure 7**). At 300 MPa, model results are in close agreement with the clinopyroxene-melt *P-T*-H_2O estimates, and with the inclusion populations. For example, feldspar is not produced at 400 MPa, yet by reducing the pressure to 350 MPa, plagioclase saturates the melt at 1,010°C. Therefore, we conclude that the crystallisation of the megacrysts is best reproduced at 300 MPa pressure. Fluctuations in volatile components may also affect the fractionating assemblage. For example, the melt water content modulates the stability of plagioclase, and thermodynamic simulations at H_2O <2 wt.% expand the stability of feldspar and limit the production of apatite. Fluxing with CO_2 can also dehydrate the melt (Spilliaert et al., 2006) promoting crystallisation of plagioclase (Cashman and Blundy, 2013), and modulating the texture and composition of the crystallising assemblage (Humphreys et al., 2009; Giuffrida et al., 2017). This is particularly relevant at Stromboli, where magmas are enriched in CO_2 relative to typical arc systems (Aiuppa et al., 2010; Allard, 2010).

To the best of our knowledge, *P-T*-H_2O estimates from this study are the first set of comprehensive mineral-melt equilibrium constraints on clinopyroxene crystallisation at Stromboli (**Figure 8**). Thermodynamic modelling supports crystallisation of the megacrysts and their inclusions from a relatively evolved shoshonitic melt equilibrating at ∼300 MPa, 1,080°C, 2 wt.% H_2O, and NNO-buffered conditions (**Figure 7**). Our pressure results reflect the relatively high Na_2O and Al_2O_3 concentrations in the clinopyroxene megacrysts (**Figure 7**), consistent with the increasingly compact structure of the mineral at higher pressures (Blundy et al., 1995; Nimis, 1995; see **Supplementary File 1**). Assuming a mean rock density of 2,700 kg/m^3 for the crust at Stromboli (Allard, 2010), clinopyroxene-melt pressure results of 316 ± 33 MPa indicate depths of crystallisation of 11.9 ± 1.2 km, below the major mid-crustal discontinuity beneath the volcano (∼10 km; Morelli et al., 1975). These estimates will be discussed in the context of the plumbing system in section New Insights Into Plumbing System Architecture.

DISCUSSION

Multi-Method Approach to Elemental Mapping

The sharp chemical contrasts revealed within seemingly homogeneous megacrysts (**Figures 4–6**) illustrate the potential of micro-chemical mapping as a new petrological tool with which to better understand the compositional and textural complexities of igneous crystals, as well as other geological materials (e.g., Burger et al., 2015, 2017; Ubide et al., 2015; Gundlach-Graham et al., 2018). The combination of major element maps obtained via electron microprobe, with trace element maps acquired by LA-ICP-QMS, and the significantly extended multi-element mapping capability of LA-ICP-TOFMS, provides a powerful means to interrogate magmatic histories recorded in clinopyroxene megacrysts (**Figures 4–6**). Here we discuss the main benefits and drawbacks of the mapping approaches, and highlight key textural and compositional information extracted using each method.

Most notably, the outstanding record of zoning patterns visualised with the TOF maps provides fundamental navigation for subsequent analyses and crystal-scale interpretations. The icpTOF instrument mapped the mass spectrum from ^{23}Na to ^{238}U on entire, mm-sized crystal sections in as little as 1 h (**Table 1**). Together with our crystallographically controlled

sectioning approach, LA-ICP-TOFMS maps provide invaluable rapid insights not only into the general core-to-rim major and trace element zonation, but also into the complex sectioning effects of hourglass and prism sectors (**Figures 3**, **5**, **6**).

LA-ICP-QMS mapping generated trace element images of increased-resolution and -sensitivity that revealed fine textural details and subtle compositional variations (e.g., **Figure 4**). Compared to the TOF approach, conventional LA-ICP-QMS mapping is limited by the number of analytes and requires longer analytical run times (**Table 1**). Relative to the 1 laser spot = 1 pixel approach used with the icpTOF (Burger et al., 2015; Bussweiler et al., 2017), the LA-ICP-QMS spot-overlapping technique improves spatial resolution at a given spot size and, therefore, the LA-ICP-QMS maps were preferred to undertake precise thickness measurements on Cr maps for timescale estimates (section Crystal Storage and Mobilisation Timescales). We note that the benefit of spot-resolved imaging is that each pixel is exactly in the right location and that the rastering approach involves the risk of signal smearing and/or spectral skew. However, Ubide et al. (2015) showed that for modern analytical systems with fast washout times, and limited total dwell cycles (dictated by the repetition rate), the spatial resolution of the rastering approach is better than the spot size. The improved sensitivity of the LA-ICP-QMS technique employed here is exemplified in maps showing mild compositional contrasts such as Ni (**Figure 4**), which remained undetected with the TOF method.

The spatial resolution of laser-based approaches is primarily controlled by the spot size, which was set at 20 μm for all the analyses in this study (**Table 1**). Importantly, vertical sample "destruction" in mapping experiments is negligible compared to traditional spot analysis, and has been quantified at <1 μm depth relative to the original sample surface in clinopyroxene LA-ICP-QMS maps (Ubide et al., 2015). Hence, samples can be mapped multiple times and then re-polished for traditional petrography or electron beam techniques.

Electron microprobe maps on large areas of the megacrysts (**Figure 4**, **Supplementary Figure 1**) provided general sectoral variations as well as valuable information on the occurrence and distribution of inclusion populations. Whilst more time consuming and less sensitive for trace elements than laser mass spectrometry methods, electron-based imaging techniques are commonly available to petrologists and mineralogists and provide a powerful approach for resolving micro-chemical complexities in major and minor elements.

Dynamic Crystallisation of Clinopyroxene Megacrysts

The megacrysts are markedly euhedral and their chemical complexity is only revealed via micro-chemical imaging. Interestingly, compositional zoning patterns vary according to element group. A large proportion of major elements appear relatively homogeneous to mildly sector zoned, whereas minor and trace elements show decoupled distributions in oscillatory zones and/or sectors. Within the overall homogeneity, Al, Ti, (Fe), and highly charged trace cations including V, REE, and HFSE are enriched in prism sectors relative to hourglass sectors. This distribution agrees with that observed in sector zoned clinopyroxenes at Mt. Etna (Downes, 1974; Duncan and Preston, 1980; Ubide et al., 2019) and other volcanic systems world-wide (Hollister and Gancarz, 1971; Ferguson, 1973; Leung, 1974). In a recent study on major and trace element zoning of sector zoned clinopyroxene, Ubide et al. (2019) demonstrated that sector zoning is strongly dependent on the charge/size of a given cation and its ability to charge-balance the clinopyroxene structure after incorporation of Al^{3+} in tetrahedral substitution for Si^{4+}. The authors showed that sector zoning can develop under conditions of low undercooling, and proposed that the extent of sectoral partitioning might be related to the degree of undercooling. Interestingly, sectoral partitioning is significantly stronger in Etnean phenocrysts than in Stromboli megacrysts. The differential partitioning of hourglass and prism sectors in Etna phenocrysts is typically twice as large compared to Stromboli megacrysts, and the compositions of prims sectors {100}, {110}, and {010} are distinct from each other at Etna but indistinguishable at Stromboli (compare Figure 6 in Ubide et al., 2019 with **Figure 7**, this study). In this regard, the comparatively mild sector zoning of the studied megacrysts from Stromboli could be linked to very low degrees of undercooling and crystallisation conditions very close to thermodynamic equilibrium. In fact, all the sectors in the megacrysts are in equilibrium with shoshonite melt (**Supplementary Figure 5**). Furthermore, very low undercooling conditions are consistent with the formation of large megacrysts under growth-dominated crystallisation, whereas higher undercooling conditions would favour smaller phenocrysts through nucleation-dominated crystallisation (Kirkpatrick, 1977; Landi et al., 2019). The origin of the mild undercooling conditions has important implications for the interpretation of crystallisation dynamics. One possible explanation could be megacryst crystallisation during very slow magma ascent. However, given the protracted magma storage suggested by the large size of the megacrysts, we consider crystallisation at the margin of a reservoir, which could undergo convection (e.g., Welsch et al., 2009), as a more plausible hypothesis. Such a scenario would impose low, relatively constant undercooling conditions that agree with the mild sector zoning ubiquitous across megacryst cores, mantles, and rims.

The homogeneous major element data recovered for crystal and melt portions across the clinopyroxene megacrysts indicate that crystallisation was supplied by continuous input of uniform shoshonitic melts, as suggested by crystal size distribution analysis of the products of historical eruptions at Stromboli (e.g., Armienti et al., 2007). The megacrysts may therefore offer a record of incremental magma body growth (Cashman and Blundy, 2013), where successive inputs of magma of buffered bulk composition replenished and interacted with prior melts and crystals. Mineral inclusions are abundant across the megacrysts (**Figures 4**–**6**) suggesting that new magma inputs promoted heterogeneous nucleation of clinopyroxene and other phases on pre-existing clinopyroxene crystals (Kirkpatrick, 1977). To investigate subtle modulations in the history of melt compositions involved in clinopyroxene growth, we hereafter deconstruct the Cr record across the megacrysts. As a slow

diffusing and highly compatible cation in the clinopyroxene structure (D'Orazio et al., 1998; Costa and Morgan, 2011), chromium defines fine concentric variations with only minor sector partitioning (Ubide et al., 2019).

Some of the megacrysts contain Cr-rich antecryst cores (e.g., **Figure 5**) that lack sector zoning and could have formed under very slow crystallisation conditions before being partially dissolved and incorporated into new shoshonitic melt. Because antecryst cores lack internal features, however, we cannot rule out the possibility of diffusive resetting during protracted storage at magmatic temperatures (e.g., Costa and Morgan, 2011). Whilst similar to other clinopyroxene compositions in major elements, the Cr-rich antecryst cores lack apatite inclusions, suggesting crystallisation from a relatively mafic and volatile-poor shoshonitic melt. Resorbed cores with distinct chemical signatures have also been described in the Pizzo high-K subgroup (Francalanci et al., 2014), as well as in the Post-Pizzo to Present-day sequence (Petrone et al., 2018), and during the most recent activity of Stromboli (Francalanci et al., 2005, 2012; Bragagni et al., 2014). In all these previous studies, the antecryst cores have been interpreted as older cumulates derived from the crystal mush zone, recycled or "cannibalized" (Cashman and Blundy, 2013) by volatile-rich, hot, mafic magmas.

Megacryst cores and mantles differ in the nature of their concentric zonations. The mantles show fine Cr oscillations that could be linked to changes in intensive or extensive parameters through time. However, the euhedral textures of concentric zones, together with the compositional consistency of mineral and melt inclusions, indicate that such changes were relatively minor. A plausible explanation is continued replenishment of the megacryst-crystallising reservoir with shoshonite-buffered magmas, followed by minor magma fractionation, reduction of Cr levels and further replenishment. Additionally, convection of the megacrysts within a chemically heterogenous reservoir could result in crystallisation from slightly different melts through time. It is interesting that the megacryst cores do not show such inner oscillations, however they are also sector zoned. If sector zoning relates to cooling rate (Welsch et al., 2009, 2016; Garrison et al., 2018; Ubide et al., 2019), then the thermal path of cores and mantles should be the same. Therefore, the cores and mantles could have crystallised at the margin of a reservoir and: (a) the reservoir was relatively stable during the crystallisation of the cores and was repeatedly replenished during the crystallisation of the mantles; or (b) the megacryst convected within an initially homogeneous reservoir that became compositionally zoned with time. Recharge events are common drivers of convective dynamics in magmatic reservoirs (Bergantz et al., 2015; Landi et al., 2019; and references therein) and a recent investigation on the textural and compositional records of K-feldspar megacrysts from Southern Tuscany (Italy) by Landi et al. (2019) suggested that repeated influx of hot magma can, in fact, favour the growth of large megacrysts.

The primary distinguishing feature of megacryst rims is their Cr-rich composition (**Figures 4–6**). This applies not only to clinopyroxene rims, but also to rim-hosted titanomagnetite inclusions, which are more Cr-rich than core- and mantle-hosted titanomagnetites. Such variations, coupled with milder enrichments in Ni and depletions in incompatible elements, suggest crystallisation from a more mafic melt (Streck, 2008; Ubide and Kamber, 2018). Given the lack of apatite inclusions at megacryst rims (e.g., **Figure 4**) and adhering groundmass, the recharge magma was possibly less volatile-rich than the resident magma. Chromium-rich rims occur in all the studied crystals, implying ubiquitous mixing shortly before eruption (e.g., Kent et al., 2010). Mafic recharge and mixing may therefore represent the eruption-triggering mechanism (Ubide and Kamber, 2018). Numerical modelling has shown that stirring and swirling of crystals upon recharge can generate a variety of zonation patterns (Bergantz et al., 2015). Such reservoir dynamics involving interaction between crystals and melts could well explain the spectrum of rim textures recorded in the megacrysts, including multiple oscillations and discontinuous dissolution between Cr-poor and subsequent Cr-rich layers (e.g., **Figure 4**). Still, the major element compositions of the clinopyroxene rims and rim-hosted mineral and melt inclusions are consistent with those of core, mantle and groundmass regions, suggesting mixing between compositionally similar shoshonitic melts. In a study of clinopyroxene megacrysts from the infamous 1669 eruption at Mt. Etna, Magee et al. (in press) have suggested that the pressure oversaturation of the system leading to the onset of eruption could have been triggered by a large-volume mafic injection, and not necessarily by a major compositional change in the intruding magma. Similarly, the recharge that tipped the Stromboli megacrysts to erupt was likely "cryptic," only compositionally distinct at the trace element level (e.g., Magee et al., in press).

Crystal Storage and Mobilisation Timescales

The relative sizes of growth zones in the megacrysts (e.g., thin rims) suggest rapid melt mobilisation upon recharge and mixing, in contrast to the longer timescales of crystal residence implied by large megacryst cores and mantles. Chromium zonations are very sharp in spite of the lack of major element variation, which precludes application of Fe-Mg diffusion chronometry (e.g., Costa and Morgan, 2011; Petrone et al., 2018). Experimental data on crystallisation kinetics of Stromboli and Etna basalts show that at low degrees of undercooling, crystal growth rates can be considered constant (Vona and Romano, 2013). Therefore, the thickness of crystal zones can be used to approximate the time of crystallisation in deep magmatic environments, provided that crystal growth rates are well-constrained and the growth of a given mineral zone can be considered continuous (Ubide and Kamber, 2018). The megacrysts studied here have polyhedral shapes and major element compositions that indicate crystallisation in deep-seated reservoirs, under constant P-T-H_2O conditions from core to rim (**Figure 8**). Melt inclusions trapped throughout megacryst growth have similar compositions to groundmass glasses, including incompatible and slow diffusing elements such as P and Al (**Supplementary Table 7**). This observation

implies that the melt inclusions are not the trapped remnants of a liquid boundary layer surrounding rapidly growing clinopyroxenes, which would be enriched in incompatible elements relative to the bulk melt composition (Baker, 2008). Thus, we assume that the megacrysts formed at depth under conditions of low undercooling, supported by presence of only weak sector zoning.

Studies on clinopyroxene growth kinetics in alkaline basaltic melts from Mt. Etna, conducted both in experiments (Orlando et al., 2008; Mollo et al., 2013) and through crystal size distribution analyses of natural products (Armienti et al., 2013), have constrained clinopyroxene growth rates on the order of 10^{-8} cm/s at low degrees of undercooling ($\Delta T <$ 10–20°C). Because the rims record the final crystallisation stage and potentially the eruption trigger, we assume that they grew continuously and immediately prior to eruption (Ubide and Kamber, 2018). We, therefore, apply the 10^{-8} cm/s growth rate to the thicknesses measured across crystal rims to estimate the timescales of magma mixing and mush mobilisation upon magma intrusion. Results can be discussed as recharge-to-eruption timescales under the assumption that magma ascent is rapid to instantaneous. Indeed, olivine growth during the Present-day paroxysms at Stromboli suggests magma ascent from 350 MPa within a few hours to a few tens of hours (Bertagnini et al., 2003). To minimise the effect of differential growth in different crystallographic orientations, we limit our timescales to measurements across the prism sectors {100}, {010}, and {110}, and disregard measurements across the faster growing hourglass sectors {-111} as they yield longer timescales than the prism group. Results for 58 rim thicknesses across prism sectors on 11 megacrysts and 20 crystal sections converge at 200 ± 99 μm, returning timescales of mixing and evacuation following recharge of 22 ± 10 days. This estimate is of the same order of magnitude as maximum mixing, stirring and triggering timescales of 10 days obtained from thickness measurements on clinopyroxenes from younger Stromboli products (Post-Pizzo to Present-day activity; Petrone et al., 2018). In the Present-day shallow plumbing system, plagioclase crystal size distributions in natural scoriae combined with growth rates from decompression experiments indicate minimum mixing-to-equilibration timescales of hours to days (Agostini et al., 2013).

The recharge-to-eruption timescales, whilst dependent on the veracity of growth rate estimates, are in good agreement with results of numerical simulations of magma recharge in basaltic mush systems, which show that mixing processes that precondition magmas for eruption can operate on timescales of days-weeks (Schleicher et al., 2016). These authors quantified that the volume of magma mobilised by the intruding melt depends on the mass flux of the intrusion, further supporting the notion that compositionally similar but volumetrically significant magma recharge has the potential to trigger eruption.

Growth prior to the final recharge event was likely discontinuous, and we lack constraints on potential hiatuses in crystallisation during storage, violating the premise of continuous growth required for timescale calculations. We also note that repeated replenishment of the crystallising reservoir with hot magma could have led to dissolution episodes (see also Landi et al., 2004, 2008; Armienti et al., 2007). The fine oscillatory zoning of megacryst mantles may reflect repeated mafic injections; however, dissolution features are uncommon between growth layers (e.g., **Figures 4–6**), except around antecrysts. In any case, it is reasonable to assume that crystallisation of the core-mantle portions of the megacrysts took place over protracted periods of magma storage. Indeed, previous studies obtained decadal-centennial timescales of magma residence, based on: (1) Fe-Mg diffusion modelling of clinopyroxene zoning profiles from the Post-Pizzo and Present-day activity (typically 1–50 years after crystallisation of diopsidic bands, and up to 150 years at the initial phase of the Post-Pizzo sequence; Petrone et al., 2018); (2) Sr isotope data on clinopyroxenes from the twentieth century activity (19 years; Francalanci et al., 1999); and (3) time series analysis of U-series disequilibria of 1996–2007 products (<55 years in the deep LP reservoir and 2–10 years in the shallow HP reservoir; Bragagni et al., 2014).

New Insights Into Plumbing System Architecture

The plumbing system feeding Stromboli volcanism has been extensively studied from volcanological, petrological and geochemical perspectives (cf. reviews by Francalanci et al., 2013; Cashman and Edmonds, 2019 and references therein). The feeder system is depicted as a vertically extended mush column that, at present, has an open-conduit configuration feeding the unique, constant eruptive activity at the summit craters (e.g., Métrich et al., 2010). Steady-state Strombolian explosions produce black scoriae deposits with high phenocryst (HP) contents (up to ca. 50 vol.% of crystals; Armienti et al., 2007) and low volatile contents (<1.5 wt.% H_2O; Aiuppa et al., 2010; Métrich et al., 2010). Periodically, the persistent Strombolian activity is punctuated by more energetic explosive eruptions (paroxysms) that eject light-coloured ("golden") pumices with low phenocryst (LP) contents (<5–10 vol.% of crystals; Armienti et al., 2007) and high volatile contents (2.5–3.5 wt.% H_2O and 0.15–0.2 CO_2; Aiuppa et al., 2010; Métrich et al., 2010), mingled with the regular HP scoriae. More sporadically (every 4 years since 1888; Aiuppa et al., 2010), effusive episodes produce lava flows with HP petrological characteristics (Armienti et al., 2007). At present, the LP magmas have more mafic compositions than HP magmas and are interpreted to tap deeper, undegassed magmas that travel quickly to the surface (Bertagnini et al., 2003; Métrich et al., 2010). According to olivine-hosted melt inclusions (Aiuppa et al., 2010; Métrich et al., 2010), HP and LP magmas are fed by magma bodies located at 50–100 MPa (2–4 km depth below the summit vents) and 190–260 MPa (7–10 km depth below the summit vents), respectively. The shallow magma ponding zone at 2–4 km is supported by geodetic data (Bonaccorso et al., 2008) and plagioclase compositions (Landi et al., 2004; Francalanci et al., 2005). This depth range coincides with the depth of the interface between volcanic rocks and the basement (2.4–3.5 km; Di Roberto et al., 2008), and connects with the upper feeder dyke-conduit (Burton et al., 2007). Meanwhile, the location of the LP reservoir is consistent

with a major mid-crustal discontinuity at 10 km (Morelli et al., 1975) and with precursory seismic signals and geochemical anomalies in crater plume emissions prior to recent paroxysmal activity (Pino et al., 2011).

Over time, different magma reservoirs have been tapped due to edifice collapse, however, two common levels of magma storage (similar to the current HP-LP double-tier architecture described above) have persisted throughout the entire known history of the volcano, located at ∼3 and ∼9–11 km depth (Francalanci et al., 2013, 2014 and references therein). In Pizzo times, the deep and shallow reservoirs were independent, and fed contemporaneous high-K and shoshonite products, respectively (Francalanci et al., 2014). While the Pizzo-shoshonite magma chamber was periodically recharged and still persists (HP reservoir), Francalanci et al. (2014) stressed that there is no evidence of a clear high-potassium signature in the products erupted after the Pizzo period. All erupted magmas postdating Pizzo activity are invariably shoshonitic basalts (Petrone et al., 2018), and only a minor high-K component has been identified in the LP magmas (Francalanci et al., 2013, 2014). The proto-LP-HP configuration and connectivity was established as early as the Post-Pizzo era (Petrone et al., 2018) and syn-eruptive mixing has persisted until today (Francalanci et al., 2013).

We find that the megacrysts studied here are compositionally akin to the Pizzo shoshonite subsystem (**Figure 7**), yet they return significantly deep conditions of crystallisation (∼300 MPa; **Figure 8**) relative to the Present-day HP reservoir (**Figure 9**). In detail, the majority of megacryst domains are compositionally indistinguishable from smaller pyroxenes hosted in Pizzo shoshonites (**Figure 7**, right panels). Similarly, the megacryst-hosted melt inclusions have a compositional affinity with the glass compositions in the shoshonite subgroup (Francalanci et al., 2014; **Supplementary Figure 4**). Hence, the megacrysts are inferred to have crystallised from Pizzo shoshonite melt, but at relatively high pressure, below the depth of the 10 km mid-crustal discontinuity beneath Stromboli (Morelli et al., 1975; **Figure 9**). The megacrysts grew from relatively evolved magma at temperatures of ∼1,080°C, water contents of ∼2 wt.% H2O, and NNO-buffered conditions [see section Estimating Clinopyroxene Crystallisation Conditions (*P*-*T*-H2O)]. Tests for equilibrium between clinopyroxene and melt compositions confirm the reliability of our estimates (**Supplementary Figure 5**), which were obtained with recently optimised clinopyroxene-melt *P*-*T*-H_2O calibrations (Mollo et al., 2018), further adjusted to approach ideal equilibrium conditions (**Figure 8**), and corroborated by thermodynamic simulations using Rhyolite-MELTS (Gualda et al., 2012; **Figure 7**). The implications of our estimates may therefore be discussed in the context of the plumbing system feeding volcanism at Stromboli.

Our pressure estimates at ∼300 MPa agree with the deepest roots of the plumbing system at Stromboli probed by melt inclusions (Aiuppa et al., 2010). It is important to stress that the pressures (depths) deduced from olivine-hosted melt inclusions only record the conditions of olivine crystallisation. In contrast, clinopyroxene-hosted melt inclusions have not provided reliable pressure constraints at Stromboli (Métrich et al., 2010). These authors noted that magma batches feeding olivine growth at current HP-LP reservoirs necessarily rise from deeper levels, and our data suggest clinopyroxene megacrysts crystallised at ≥10 km in Pizzo times. Clinopyroxene is known to crystallise from basaltic magmas across a wide range of pressures (e.g., Putirka, 2017) and can dominate the deep plumbing system of alkaline and hydrous volcanoes, for example Mt. Etna (Armienti et al., 2013; Mollo et al., 2015; Ubide and Kamber, 2018). At Stromboli, ponded partial melts have been resolved down to the base of the 17-km thick continental crust, where a low *Vp* and *Vs* volume has been seismically detected (Barberi et al., 2007).

Plagioclase stability expands under water-poor conditions and becomes dominant upon degassing of water-rich magmas at shallow depth (e.g., Francalanci et al., 2004; Landi et al., 2004, 2008; Giacomoni et al., 2014). At Stromboli, the transition from closed- to open-system degassing (and LP to HP magma in the current plumbing system) occurs at shallow depths of 2–4 km below summit vents (Aiuppa et al., 2010), with plagioclase becoming ubiquitous when the H_2O concentration of the melt reaches ≤1 wt.% (Landi et al., 2004). Hence, we propose that the vertical configuration of the plumbing system at Stromboli in Pizzo times could have been stratified into mid-crustal clinopyroxene-rich mushes transitioning to olivine crystallisation and finally plagioclase dominance in shallow degassing reservoirs (**Figure 9**), similar to other H_2O-rich basaltic systems such as Mt. Etna (Armienti et al., 2013; Mollo et al., 2015; Ubide and Kamber, 2018; Magee et al., in press). The implications of deep clinopyroxene crystallisation must be considered when calculating magma ascent rates (e.g., Petrone et al., 2018) and in volcano monitoring efforts (including seismic crises; e.g., Pino et al., 2011). Compared to the megacrysts, recent clinopyroxenes have relatively lower Na_2O and Al_2O_3 contents (**Figure 7**, right panels) and thus may have crystallised under shallower conditions (e.g., Nimis, 1995). Therefore, further barometric evidence from clinopyroxenes across the eruptive history of Stromboli is needed to test if the stratified plumbing system configuration inferred for the Pizzo megacrysts also controlled other Pizzo products and later eruptive periods, up until Present-day activity.

Two Millennia of Magmatic Invasion Leading to Steady-State Activity

Stromboli affords an opportunity to explore the evolution of an active volcano on short, geological to historical, and even human timescales. The bulk rock compositions of the products erupted in the last 13 ka (from the onset of Epoch 5-Neostromboli through to Epoch 6-Recent Stromboli, including Pizzo to the Present-day activity; **Figure 1**) show a progressive decrease in SiO_2, incompatible elements (e.g., Rb, Zr) and $^{87}Sr/^{86}Sr$ with time, coupled with an increase in MgO and $^{143}Nd/^{144}Nd$ (Francalanci et al., 2013 and references therein). This magmatic evolution indicates a progressive change to more primitive melts with distinct source characteristics. On shorter timescales, whole rock and clinopyroxene compositional variations from Post-Pizzo and Present-day products are consistent with the time progression of the Stromboli system toward more mafic compositions (Petrone et al., 2018). On even shorter (decadal)

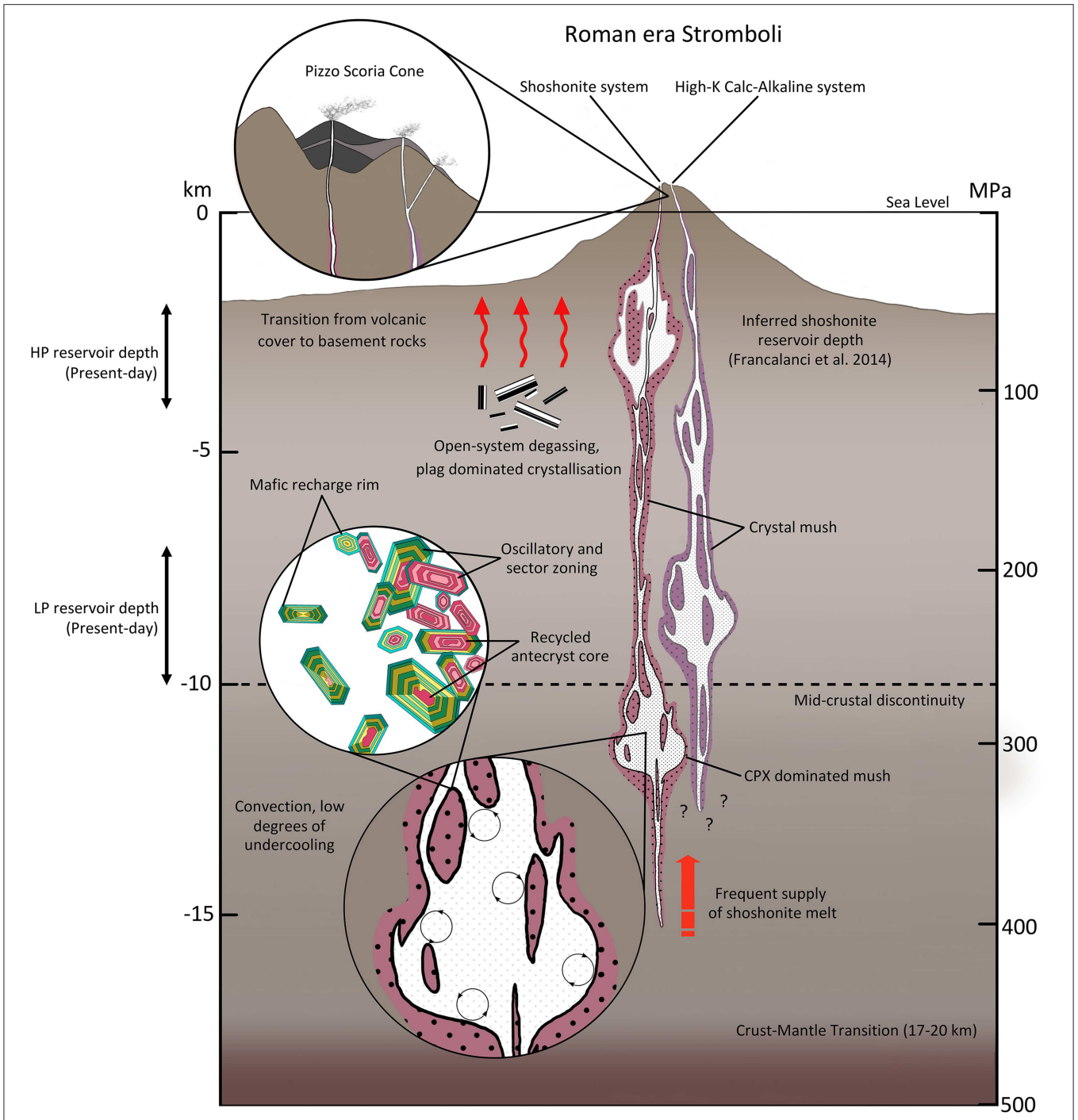

FIGURE 9 | Working model for the extended plumbing system at Stromboli volcano during Pizzo (Roman) times. Clinopyroxene megacrysts crystallised below the 10 km mid-crustal discontinuity (Morelli et al., 1975), deeper than the reservoir depths inferred for Pizzo, Post-Pizzo, and Present-day activity based on olivine-hosted melt inclusions (Aiuppa et al., 2010; Métrich et al., 2010; Francalanci et al., 2013; double-headed arrows mark the depth ranges of current HP-LP reservoirs). The megacrysts grew from incremental replenishments and convection of shoshonite magma under conditions of low undercooling, generating mild concentric and oscillatory zonations which sometimes overgrow inherited cores. As suggested by Francalanci et al. (2014), the Roman-age feeding systems of the shoshonite subgroup (studied through clinopyroxene megacrysts here) and the high-K calc-alkaline subgroup were independent. The magnifying glass at the top highlights eruptive relationships between the two magmas. The lack of Mg-rich (diopsidic) bands in the studied megacrysts, typical of Post-Pizzo and Present-day clinopyroxenes (Petrone et al., 2018), suggests that the inception of the steady-state activity may be related to the invasion of the plumbing system with mafic magma in the last two millennia, after eruption of the megacrysts. The crust-mantle transition under Stromboli has been inferred at 17 km (Panza et al., 2007; Métrich et al., 2010) to 20 km (Laiolo and Cigolini, 2006), and the interface between volcanic rocks and the basement lies at about 2.4–3.5 km depth (Di Roberto et al., 2008); both transitions are denoted by transitional grading in the figure.

timescales, Sr isotope systematics in bulk rocks decreased significantly from the 1980s until 2000 (Francalanci et al., 2004). Within that period, micro-drilled portions of clinopyroxene and plagioclase crystals indicated a rapid decrease of $^{87}Sr/^{86}Sr$ in crystal mantles followed a mild increase at the rims, implying replenishment with mafic magma followed by mixing prior to eruption (Francalanci et al., 2005). Here, we use the clinopyroxene compositional variations to track changes in magma composition back to the Roman era (Pizzo, 2.4–1.8 ka).

The Pizzo megacrysts lack a key feature of clinopyroxenes from more recent eruptions. Clinopyroxene crystals from Post-Pizzo and Present-day activity show "diopsidic bands" identified as darker grayscale contrast zones in BSE images (lighter coloured under plane polarised light), with up to $Mg\#_{\sim 90}$ (Francalanci et al., 2004, 2005; Landi et al., 2006; Armienti et al., 2007; Petrone et al., 2018; **Figure 7**, right panels) that record the intrusion of hot and significantly more mafic magma into the system (Petrone et al., 2018). The diopsidic composition is typically found as thin, euhedral mantle (intermediate) zones, but can also occur as resorbed cores or at crystal rims (Francalanci et al., 2004, 2005; Landi et al., 2006; Armienti et al., 2007; Petrone et al., 2018). In contrast, the megacrysts studied here have remarkably homogeneous major element compositions with $Mg\#_{71-78}$. A compilation of clinopyroxene compositions from Pizzo (shoshonite and high-K subgroups; Francalanci et al., 2014), Post-Pizzo and Present-day activity (Francalanci et al., 2005; Petrone et al., 2018) shows a distinct Mg#-rich group (not present in Pizzo megacrysts) that becomes more prevalent through time (**Figure 7**). During the Pizzo era, shoshonite-hosted crystals show similar compositions to the megacrysts studied here, whereas high-K basalt-hosted clinopyroxenes show an incipient increase in Mg#. The diopsidic compositions become more frequent through Post-Pizzo and Present-day activity products (Petrone et al., 2018). Even though all compositions generate a common evolutionary path in SiO_2, TiO_2, and Na_2O vs. MgO bivariate plots, the low-Mg# augitic compositions and high-Mg# diopsidic compositions are separated by steps in Al_2O_3, CaO, and Cr_2O_3 vs. MgO (**Figure 7**, right panels) that suggest a change in the crystallisation environment (see also Francalanci et al., 2004). Interestingly, Mg-rich zones are relatively enriched in CaO (**Figure 7**), a feature mirrored in bulk rock compositions (Bertagnini et al., 2003). Hence, according to the compiled database, the mafic magma invading Stromboli in historical times may have first appeared as high-K magma in Pizzo times, when the megacryst environment remained uninvaded. The data suggest a genetic link between the Pizzo high-K magmas and the invading magma, which is intriguing because the intruding magma reported from Post-Pizzo times is shoshonitic in composition (Francalanci et al., 2013; Petrone et al., 2018). However, Francalanci et al. (2014) noted that while the high-K component has not directly erupted after Pizzo times, it has been present for a long period in the Stromboli plumbing system and could be undergoing dormant recharge. Tentatively, the clinopyroxene data may point to the role of a minor (diluted) high-K component in the Present-day shoshonite magmas, as suggested by Francalanci et al. (2013). In line with the idea of enhanced mixing in the feeder system through time, Francalanci et al. (2004) reported that clinopyroxenes from eruptions spanning the twentieth century are remarkably uniform in major and minor elements.

It is pertinent to observe that the inception of steady-state activity at Stromboli (at least since Post-Pizzo times; Petrone et al., 2018) is in agreement with the invasion of the plumbing system with distinctly mafic magma, as recorded by clinopyroxene crystals (Petrone et al., 2018; **Figure 7**). Bulk rock Sr isotope ratios become progressively less radiogenic from Pizzo shoshonite products up until Present-day activity, and bulk rock major elements record a mafic trend since Post-Pizzo times (Petrone et al., 2018), shortly after the eruption of the megacrysts. Timescales of magma mixing and crystal mobilisation upon recharge obtained in this study (22 ± 10 days, Pizzo) are within error of those of Petrone et al. (2018; up to 10 days, Post-Pizzo—Present-day). Although it may appear that the triggering timescales have shortened somewhat from Pizzo to Post-Pizzo and Present-day activity, further data are required to establish if the invading mafic magma has brought about increased eruption-triggering efficiency. Similarly, Petrone et al. (2018) highlighted that crystal residence timescales have decreased from the initial phase of the Post-Pizzo activity onwards. In agreement with the hypothesis of progressive invasion, Petrone et al. (2018) found that the top of the Post-Pizzo sequence contains abundant clinopyroxenes with multiple diopsidic bands, suggesting the occurrence of more frequent replenishment events than at the inception of Post-Pizzo activity, as well as a potential link between injections of new recharging magma and eruption frequency, as suggested for the persistent Present-day activity (Taddeucci et al., 2013).

In their Sr-isotope study of recent eruptions, Francalanci et al. (2005) linked the $^{87}Sr/^{86}Sr$ decrease in scoria and lavas from ∼1980 to greater volumes of recharge magma in the volcano plumbing system and increased intensity of Strombolian activity prior to the 1985 lava eruption. Here, the compilation of clinopyroxene major element data suggests that the inception of the steady-state activity might be directly related to the invasion of the plumbing system with mafic magma on historical timescales (from the Roman era until today). A similar relationship between magma invasion and enhanced eruptive activity was observed on decadal timescales for the recent enhanced volcanism at Mt. Etna (Cannata et al., 2018; Ubide and Kamber, 2018). The latter study showed that Cr zonations in clinopyroxene can hold detailed records of magma pathways through volcanic systems, and our compiled Stromboli dataset shows that diopsidic bands are clearly enriched in Cr_2O_3 (**Figure 7**). Further inspection of the textural and chemical budgets of clinopyroxenes in recent Stromboli products holds promise to help build an updated view of the feeder system, track its evolution through time and explore relationships with changes in eruptive style, all of which are important for volcano monitoring efforts.

CONCLUSIONS

A detailed understanding of clinopyroxene records opens a new perspective into the study of dynamic crystallisation and the space-time evolution of magmatic plumbing systems. We have investigated the textural and compositional complexities

of Roman era (2.4–1.8 ka; Pizzo) megacrysts from Stromboli volcano using a crystallographically controlled approach, providing petrological constraints that can be further tested on clinopyroxenes from more recent (and older) eruptions, as well as on smaller Pizzo phenocrysts. We conclude that:

- High-resolution major and trace element mapping constitutes an exciting petrological tool for the study of magmatic records from a combined textural-compositional perspective. In particular, laser ablation time-of-flight (LA-ICP-TOFMS) mapping provides very rapid visualisation of the chemical complexity of large sample materials, for a wide range of major and trace elements.
- Sector-zoned crystals provide unparalleled insight into the study of crystallisation dynamics; low charge cations (Cr, Ni; oscillatory zoned) carry information on melt history whereas Al and high charge cations (e.g., HFSE; sector zoned) carry information on cooling history (cf. Ubide et al., 2019). The Pizzo megacrysts show very mild oscillatory and sector zoning, most clearly discernible at the trace element level. Megacryst growth is interpreted in the context of incremental recharge by pulses of shoshonite melt and associated convection, generating a protracted crystallisation environment with low degrees of undercooling.
- Barometric, thermometric and hygrometric models indicate crystallisation under relatively constant P-T-H_2O conditions, at depths below the 10 km mid-crustal discontinuity beneath Stromboli. We suggest a stratified plumbing system architecture where clinopyroxene crystallisation dominates at depth and olivine-plagioclase crystallise at shallower depths from increasingly degassed melts. Deep storage and crystallisation have not previously been identified at Stromboli, and future work will investigate if the stratified configuration is a long-standing feature of Stromboli magmas.
- Megacryst rims are not significantly distinct in terms of major elements, but have enrichments in Cr that suggest the arrival of a slightly more mafic magma prior to eruption. The thicknesses of Cr-rich rims provide an approximation of the timescales of crystal mobilisation following growth over protracted (decadal-centennial) periods. If correct, the assumed growth rates imply that the clinopyroxene megacrysts erupted very quickly (days-weeks) after magma injection and mixing.
- The Pizzo megacrysts show very constant augitic major element compositions, whereas clinopyroxenes in coeval high-K products and younger eruptive products show abundant diopsidic growth bands inferred to reflect mafic invasion of the Stromboli plumbing system on historical timescales. Mafic invasion may have driven the inception of the world-famous steady-state activity at the volcano.

DATA AVAILABILITY

Datasets for this study are included in the manuscript and the **Supplementary Files**. Data are also available on request from the corresponding author (TU).

AUTHOR CONTRIBUTIONS

TU and JC collected the samples and designed the research and CB prepared the megacrysts sections. TU and MN analysed the samples with electron microprobe, and TU, SM, and FD led subsequent data treatment and barometric, thermometric, and hygrometric modelling. Mapping experiment design and data reduction were undertaken by YB (LA-ICP-TOFMS) and JC, CB, and TU (LA-ICP-QMS). CB carried out the timescale calculations. All authors were actively involved in the discussion and interpretation of the data and participated in the preparation of the manuscript.

FUNDING

This work was supported by The University of Queensland (ECR grant UQECR1717581 and MRFF grant RM2016000555 to TU), the Australian Geoscience Council and the Australian Academy of Science (34th IGC Travel Grant to TU). We thank the HP-HT laboratory of Experimental Geophysics and Volcanology (INGV Rome) and EPOS TCS MSL for access to electron microprobe analysis. We thank TOFWERK for access to LA-ICP-TOFMS instrumentation and analytical time, and support with data handling and processing. At the University of Münster, YB gratefully acknowledges support through a Marie Skłodowska-Curie Fellowship (Project ID 746518).

ACKNOWLEDGMENTS

We thank Daniele Andronico, Chiara M. Petrone, Ruadhán Magee, Matteo Masotta, and Alessio Pontesilli for insightful discussions on Stromboli volcanism and clinopyroxene zoning. We thank Dale Harpley for help photographing the megacrysts. We thank the reviewers and editors for insightful comments which helped improve the original version of the paper.

SUPPLEMENTARY MATERIAL

The Supplementary Material for this article can be found online at: https://www.frontiersin.org/articles/10.3389/feart.2019.00239/full#supplementary-material

Supplementary Figure 1 | Major element maps of megacryst section 13C, obtained with electron microprobe.

Supplementary Figure 2 | Minor and trace element maps of megacryst section 13C, obtained with LA-ICP-QMS.

Supplementary Figure 3 | Electron microprobe traverses of clinopyroxene megacryst 31, obtained by electron microprobe (locations in **Figure 5**). The compositions of core, mantle, and rim regions are largely coincident, although crystal cores reach slightly lower Si-Mg and higher Al-Ti concentrations than mantles and rims. The antecryst core is slightly enriched in Al-Ti compared to the host clinopyroxene. In terms of sectoral variations, compositions across prism sectors {100}, {110}, and {010} are virtually homogeneous. Hourglass sectors {−111} are Mg-rich and Al-poor compared to prism sectors.

Supplementary Figure 4 | Chemical classification of melts sampled by Stromboli clinopyroxene megacrysts, including clinopyroxene-hosted melt inclusions (white circles) and glass contained in the adhering groundmass (dark circles); the matrix glass composition used for clinopyroxene-melt thermobarometry and hygrometry

(**Figure 8**) is denoted by the large square symbol. The compositional fields for all Stromboli whole rocks and Eruptive Epoch 6 whole rocks are provided for comparison (Francalanci et al., 2013). The compositional fields for glass data from Pizzo and Present-day activity products are also provided (Francalanci et al., 2014; Petrone et al., 2018). Data are plotted on an anhydrous basis. In spite of the potential inter-laboratory bias, glass compositions sampled by the clinopyroxene megacrysts are compositionally similar to Pizzo shoshonite glasses and Present-day glasses, and distinct from Pizzo high-K calc-alkaline glasses.

Supplementary Figure 5 | Clinopyroxene-melt equilibrium tests (K_D(Fe-Mg)$^{cpx-melt} = 0.28 \pm 0.08$, Putirka, 2008; $\Delta DiHd$, Putirka et al., 1996; Mollo et al., 2013; D_{Na}, Blundy et al., 1995; D_{Ti}, Hill et al., 2011; Mollo et al., 2018) indicate that all clinopyroxene compositions are in chemical equilibrium with the glass hosted in the megacrysts and adhering glassy matrix, which are all consistently shoshonitic in composition. To approach the Fe^{2+} content in the melt (to test K_D(Fe-Mg)$^{cpx-melt}$), we computed our melt composition in Rhyolite-MELTS (Gualda et al., 2012) under the NNO oxygen fugacity buffer (Métrich and Clocchiatti, 1996; Di Carlo et al., 2006) and constant *P-T* conditions of 320 MPa and 1,080°C (**Figure 8**).

Supplementary Table 1 | Stromboli clinopyroxene megacrysts analysed in this study, collected from scoria at the top of the Pizzo sequence (Eruptive Epoch 6a; Francalanci et al., 2013, 2014), at 38°47′33″N 15°12′49″E.

Supplementary Table 2 | Major element data (wt.% oxides) obtained by electron microprobe on clinopyroxene megacrysts.

Supplementary Table 3 | Major element data (wt.% oxides) obtained by electron microprobe on clinopyroxene megacryst-hosted olivine inclusions.

Supplementary Table 4 | Major element data (wt.% oxides) obtained by electron microprobe on clinopyroxene megacryst-hosted plagioclase inclusions, and plagioclase microcryts in adhering glassy tephra.

Supplementary Table 5 | Major element data (wt.% oxides) obtained by electron microprobe on clinopyroxene megacryst-hosted titanomagnetite inclusions, and titanomagnetite microcryts in adhering glassy tephra.

Supplementary Table 6 | Major element data (wt.% oxides) obtained by electron microprobe on clinopyroxene megacryst-hosted apatite inclusions.

Supplementary Table 7 | Major element data (wt.% oxides) obtained by electron microprobe on clinopyroxene megacryst-hosted melt inclusions and adhering glass.

Supplementary Table 8 | Summary of results from Rhyolite-MELTS isobaric fractionation models at 300 and 400 MPa, from 1,250 to 1,030°C. For a given fractionation (cooling) step, melt data are listed first, followed by data on fractionated clinopyroxene (where present).

Supplementary File 1 | Ubide et al. (2019) *Frontiers in Earth Science*.

REFERENCES

Agostini, C., Fortunati, A., Arzilli, F., Landi, P., and Carroll, M. R. (2013). Kinetics evolution as a probe to magmatism at Stromboli (Aeolina Archipelago, Italy). *Geochim. Cosmochim. Acta* 110, 135–151. doi: 10.1016/j.gca.2013.02.027

Aiuppa, A., Bertagnini, A., Métrich, N., Moretti, R., Di Muro, A., Liuzzo, et al. (2010). A model of degassing for Stromboli volcano. *Earth Planet. Sci. Lett.* 295, 195–204.

Allard, P. (2010). A CO_2-rich gas trigger of explosive paroxysms at Stromboli basaltic volcano, Italy. *J. Volcanol. Geotherm. Res.* 189, 363–374. doi: 10.1016/j.jvolgeores.2009.11.018

Armienti, P., Francalanci, L., and Landi, P. (2007). Textural effects of steady state behaviour of the Stromboli feeding system. *J. Volcanol. Geotherm. Res.* 160, 86–98. doi: 10.1016/j.jvolgeores.2006.05.004

Armienti, P., Perinelli, C., and Putirka, K. D. (2013). A new model to estimate deep-level magma ascent rates, with applications to Mt. Etna (Sicily, Italy). *J. Petrol.* 54, 795–813. doi: 10.1093/petrology/egs085

Baker, D. R. (2008). The fidelity of melt inclusions as records of melt composition. *Contrib. Mineral. Petrol.* 156, 377–395. doi: 10.1007/s00410-008-0291-3

Barberi, G., Zhang, H., Scarfi, L., Cocina, O., Castellano, M., Chiarabba, C., et al. (2007). Crustal evidence of a low velocity Vp and Vs volume beneath Stromboli, Italy. *Geophys. Res. Abstracts* 9:02621.

Bergantz, G. W., Schleicher, J. M., and Burgisser, A. (2015). Open-system dynamics and mixing in magma mushes. *Nat. Geosci.* 8, 793–796. doi: 10.1038/ngeo2534

Bertagnini, A., Métrich, N., Landi, P., and Rosi, M. (2003). Stromboli volcano (Aeolian Archipelago, Italy): an open window on the deep-feeding system of a steady state basaltic volcano. *J. Geophys. Res.* 108:2336. doi: 10.1029/2002JB002146

Biggs, J., and Pritchard, M. E. (2017). Global volcano monitoring: what does it mean when volcanoes deform? *Elements* 13, 17–22. doi: 10.2113/gselements.13.1.17

Blundy, J. D., Falloon, T. J., Wood, B. J., and Dalton, J. A. (1995). Sodium partitioning between clinopyroxene and silicate melts. *J. Geophys. Res. Solid Earth* 100, 15501–15515. doi: 10.1029/95JB00954

Bonaccorso, A., Gambino, S., Guglielmino, F., Mattia, M., Puglisi, G., and Boschi, E. (2008). Stromboli 2007 eruption: deflation modeling to infer shallow-intermediate plumbing system. *Geophys. Res. Lett.* 35:L06311. doi: 10.1029/2007GL032921

Borovinskaya, O., Hattendorf, B., Tanner, M., Gschwind, S., and Günther, D. (2013). A prototype of a new inductively coupled plasma time-of-flight mass spectrometer providing temporally resolved, multi-element detection of short signals generated by single particles and droplets. *J. Anal. Atomic Spectrom.* 28, 226–233. doi: 10.1039/C2JA30227F

Bragagni, A., Avanzinelli, R., Freymuth, H., and Francalanci, L. (2014). Recycling of crystal mush-derived melts and short magma residence times revealed by U-series disequilibria at Stromboli volcano. *Earth Planet. Sci. Lett.* 404, 206–219. doi: 10.1016/j.epsl.2014.07.028

Burger, M., Gundlach-Graham, A., Allner, S., Schwarz, G., Wang, H. A., Gyr, L., et al. (2015). High-speed, high-resolution, multielemental LA-ICP-TOFMS imaging: part II. Critical evaluation of quantitative three-dimensional imaging of major, minor, and trace elements in geological samples. *Anal. Chem.* 87, 8259–8267. doi: 10.1021/acs.analchem.5b01977

Burger, M., Schwarz, G., Gundlach-Graham, A., Käser, D., Hattendorf, B., and Günther, D. (2017). Capabilities of laser ablation inductively coupled plasma time-of-flight mass spectrometry. *J. Anal. Atomic Spectrom.* 32, 1946–1959. doi: 10.1039/C7JA00236J

Burton, M., Allard, P., Muré, F., and La Spina, A. (2007). Magmatic gas composition reveals the source of slug-driven Strombolian explosive activity. *Science* 137, 227–230. doi: 10.1126/science.1141900

Bussweiler, Y., Borovinskaya, O., and Tanner, M. (2017). Laser ablation and inductively coupled plasma–time-of-flight mass spectrometry—A powerful combination for high-speed multielemental imaging on the micrometer scale. *Spectroscopy* 32, 14–20.

Bussweiler, Y., Giuliani, A., Greig, A., Kjarsgaard, B. A., Petts, D., Jackson, S. E., et al. (2019). Trace element analysis of high-Mg olivine by LA-ICP-MS–Characterization of natural olivine standards for matrix-matched calibration and application to mantle peridotites. *Chem. Geol.* 52, 136–137. doi: 10.1016/j.chemgeo.2019.06.019

Cannata, A., Di Grazia, G., Giuffrida, M., Gresta, S., Palano, M., Sciotto, M., et al. (2018). Space-time evolution of magma storage and transfer at Mt. Etna volcano (Italy): The 2015–2016 Reawakening of Voragine Crater. *Geochem. Geophys. Geosyst.* 19, 471–495. doi: 10.1002/2017GC007296

Cashman, K., and Blundy, J. (2013). Petrological cannibalism: the chemical and textural consequences of incremental magma body growth. *Contrib. Mineral. Petrol.* 166, 703–729. doi: 10.1007/s00410-013-0895-0

Cashman, K. V., and Edmonds, M. (2019). Mafic glass compositions: a record of magma storage conditions, mixing and ascent. *Phil. Trans. R. Soc. A* 377:20180004. doi: 10.1098/rsta.2018.0004

Cashman, K. V., Sparks, R. S. J., and Blundy, J. D. (2017). Vertically extensive and unstable magmatic systems: a unified view of igneous processes. *Science* 355:eaag3055. doi: 10.1126/science.aag3055

Costa, F., and Morgan, D. (2011). "Time Constraints from Chemical Equilibration in magmatic crystals," in: *Timescales of Magmatic Processes: From Core to Atmosphere,* eds. A. Dosseto, S. P. Turner, and J. A. Van Orman (Hoboken, NJ: Blackwell Publishing Ltd.), 125–159. doi: 10.1002/9781444328509.ch7

Del Bello, E., Mollo, S., Scarlato, P., von Quadt, A., Forni, F., and Bachmann, O. (2014). New petrological constraints on the last eruptive phase of the Sabatini

Volcanic District (central Italy): Clues from mineralogy, geochemistry, and Sr–Nd isotopes. *Lithos* 205, 28–38. doi: 10.1016/j.lithos.2014.06.015

Di Carlo, I., Pichavant, M., Rotolo, S. G., and Scaillet, B. (2006). Experimental crystallization of a high-K arc basalt: the golden pumice, Stromboli volcano (Italy). *J. Petrol.* 47, 1317–1343. doi: 10.1093/petrology/egl011

Di Roberto, A., Bertagnini, A., Pompilio, M., Gamberi, F., Marani, M. P., and Rosi, M. (2008). Newly discovered submarine flank eruption at Stromboli volcano (Aeolian Islands, Italy). *Geophys. Res. Lett.* 35:L16310. doi: 10.1029/2008GL034824

D'Orazio, M., Armienti, P., and Cerretini, S. (1998). Phenocryst/matrix trace-element partition coefficients for hawaiite-trachyte lavas from the Ellittico volcanic sequence (Mt. Etna, Sicily, Italy). *Mineral. Petrol.* 64, 65–68. doi: 10.1007/BF01226564

Downes, M. J. (1974). Sector and oscillatory zoning in calcic augites from M. Etna, Sicily. *Contrib. Mineral. Petrol.* 47, 187–196. doi: 10.1007/BF00371538

Duncan, A. M., and Preston, R. M. F. (1980). Chemical variation of clinopyroxene phenocrysts from the trachybasaltic lavas of Mount Etna, Sicily. *Min. Mag.* 43, 765–770. doi: 10.1180/minmag.1980.043.330.10

Ferguson, A. K. (1973). On hour-glass sector zoning in clinopyroxene. *Min. Mag.* 39, 321–325. doi: 10.1180/minmag.1973.039.303.08

Fowler, S. J., Spera, F., Bohrson, W., Belkin, H. E., and De Vivo, B. (2007). Phase equilibria constraints on the chemical and physical evolution of the Campanian Ignimbrite. *J. Petrol.* 48, 459–493. doi: 10.1093/petrology/egl068

Francalanci, L., Avanzinelli, R., Nardini, I., Tiepolo, M., Davidson, J. P., and Vannucci, R. (2012). Crystal recycling in the steady-state system of the active Stromboli volcano: a 2.5-ka story inferred from *in situ* Sr-isotope and trace element data. *Contrib. Mineral. Petrol.* 163, 109–131. doi: 10.1007/s00410-011-0661-0

Francalanci, L., Braschi, E., Di Salvo, S., Lucchi, F., and Petrone, C. (2014). When magmas do not interact: paired Roman-age activity revealed by tephra studies at Stromboli volcano. *Bull. Volcanol.* 76, 1–17. doi: 10.1007/s00445-014-0884-9

Francalanci, L., Davies, G. R., Lustenhouwer, W., Tommasini, S., Mason, P. R. D., and Conticelli, S. (2005). Intra-grain Sr isotope evidence for crystal recycling and multiple magma reservoirs in the recent activity of stromboli Volcano, Southern Italy. *J. Petrol.* 46, 1997–2021. doi: 10.1093/petrology/egi045

Francalanci, L., Lucchi, F., Keller, J., De Astis, G., and Tranne, R. (2013). Eruptive, volcano-tectonic and magmatic history of the Stromboli volcano (north-eastern Aeolian archipelago. *Geol. Soc. Lond. Memoirs* 37, 397–471. doi: 10.1144/M37.13

Francalanci, L., Tommasini, S., and Conticelli, S. (2004). The volcanic activity of Stromboli in the 1906–1998 AD period: mineralogical, geochemical and isotope data relevant to the understanding of the plumbing system. *J. Volcanol. Geotherm. Res.* 131, 179–211. doi: 10.1016/S0377-0273(03)00362-7

Francalanci, L., Tommasini, S., Conticelli, S., and Davies, G. R. (1999). Sr isotope evidence for short magma residence time for the 20th century activity at Stromboli volcano, Italy. *Earth Planet. Sci. Lett.* 167, 61–69. doi: 10.1016/S0012-821X(99)00013-8

Garrison, J. M., Sims, K. W. W., Yogodzinski, G. M., Escobar, R. D., Scott, S., Mothes, P., et al. (2018). Shallow-level differentiation of phonolitic lavas from Sumaco Volcano, Ecuador. *Contrib. Mineral. Petrol.* 173:6. doi: 10.1007/s00410-017-1431-4

Gernon, T. M., Upton, B. G. J., Ugra, R., Yücel, C., Taylor, R. N., and Elliott, H. (2016). Complex subvolcanic magma plumbing system of an alkali basaltic maar-diatreme volcano (Elie Ness, Fife, Scotland). *Lithos* 264, 70–85. doi: 10.1016/j.lithos.2016.08.001

Giacomoni, P. P., Ferlito, C., Coltorti, M., Bonadiman, C., and Lanzafame, G. (2014). Plagioclase as archive of magma ascent dynamics on "open conduit" volcanoes: the 2001–2006 eruptive period at Mt. Etna. *Earth Sci. Rev.* 138, 371–393. doi: 10.1016/j.earscirev.2014.06.009

Giuffrida, M., Holtz, F., Vetere, F., and Viccaro, M. (2017). Effects of CO_2 flushing on crystal textures and compositions: experimental evidence from recent K-trachybasalts erupted at Mt. Etna. *Contrib. Mineral. Petrol.* 172:90. doi: 10.1007/s00410-017-1408-3

Gualda, G. A. R., Ghiorso, M. S., Lemons, R. V., and Carley, T. L. (2012). Rhyolite-MELTS: a modified calibration of MELTS optimized for silica-rich, fluid-bearing magmatic systems. *J. Petrol.* 53, 875–890. doi: 10.1093/petrology/egr080

Gundlach-Graham, A., Garofalo, P. S., Schwarz, G., Redi, D., and Günther, D. (2018). High-resolution, quantitative element imaging of an upper crust, low-angle cataclasite (Zuccale Fault, Northern Apennines) by laser ablation ICP time-of-flight mass spectrometry. *Geostand. Geoanal. Res.* 42, 559–574. doi: 10.1111/ggr.12233

Hendriks, L., Gundlach-Graham, A., Hattendorf, B., and Günther, D. (2017). Characterization of a new ICP-TOFMS instrument with continuous and discrete introduction of solutions. *J. Anal. Atomic Spectrom.* 32, 548–561. doi: 10.1039/C6JA00400H

Hill, E., Blundy, J. D., and Wood, B. J. (2011). Clinopyroxene-melt trace element partitioning and the development of a predictive model for HFSE and Sc. *Contrib. Mineral. Petrol.* 161, 423–438. doi: 10.1007/s00410-010-0540-0

Hollister, L. S., and Gancarz, A. J. (1971). Compositional sector-zoning in clinopyroxene from the Narce area, Italy. *Am. Mineral.* 56, 959–979.

Humphreys, M. C. S., Edmonds, M., Christopher, T., and Hards, V. (2009). Chlorine variations in the magma of Soufrière Hills Volcano, Montserrat: Insights from Cl in hornblende and melt inclusions. *Geochim. Cosmochim. Acta* 73, 5693–5708. doi: 10.1016/j.gca.2009.06.014

Jarosewich, E., Nelen, J. A., and Norberg, J. A (1980). Reference samples for electron microprobe analysis. *Geostand. Newslett.* 4, 43–47. doi: 10.1111/j.1751-908X.1980.tb00273.x

Kent, A. J. R., Darr, C., Koleszar, A. M., Salisbury, M. J., and Cooper, K. M. (2010). Preferential eruption of andesitic magmas through recharge filtering. *Nat. Geosci.* 3, 631–636. doi: 10.1038/ngeo924

Kirkpatrick, R. J. (1977). Nucleation and growth of plagioclase, Makaopuhi and Alae lava lakes, Kilauea Volcano, Hawaii. *Geol. Soc. Am. Bull.* 88, 78–84. doi: 10.1130/0016-7606(1977)88<78:NAGOPM>2.0.CO;2

Kozu, S., and Washington, H. S. (1918). Augite from Stromboli. *Am. J. Sci.* 4–45, 463–469. doi: 10.2475/ajs.s4-45.270.463

Laiolo, M., and Cigolini, C. (2006). Mafic and ultramafic xenoliths in San Bartolo lava field: new insights on the ascent and storage of Stromboli magmas. *Bull. Volcanol.* 68, 653–670. doi: 10.1007/s00445-005-0040-7

Landi, P., Francalanci, L., Pompilio, M., Rosi, M., Corsaro, A., Petrone, C. M., et al. (2006). The December 2002–July 2003 effusive event at Stromboli volcano, Italy: insights into the shallow plumbing system by petrochemical studies. *J. Volcanol. Geotherm. Res.* 155, 263–284. doi: 10.1016/j.jvolgeores.2006.03.032

Landi, P., La Felice, S., Petrelli, M., Vezzoli, L. M., and Principe, C. (2019). Deciphering textural and chemical zoning of K-feldspar megacrysts from Mt. Amiata Volcano (Southern Tuscany, Italy): insights into the petrogenesis and abnormal crystal growth. *Lithos* 324–325, 569–583. doi: 10.1016/j.lithos.2018.11.032

Landi, P., Metrich, N., Bertagnini, A., and Rosi, M. (2004). Dynamics of magma mixing and degassing in plagioclase at Stromboli (Aeolian Archipelago, Italy). *Contrib. Mineral. Petrol.* 147, 213–227. doi: 10.1007/s00410-004-0555-5

Landi, P., Métrich, N., Bertagnini, A., and Rosi, M. (2008). Recycling and "re-hydration" of degassed magma inducing transient dissolution/crystallization events at Stromboli (Italy). *J. Volcanol. Geotherm. Res.* 174, 325–336. doi: 10.1016/j.jvolgeores.2008.02.013

Leung, I. S. (1974). Sector-Zoned titanaugites: morphology, crystal chemistry and growth. *Am. Mineral.* 59, 127–138.

Longerich, H. P., Jackson, S. E., and Günther, D. (1996). Laser ablation inductively coupled plasma mass spectrometric transient signal data acquisition and analyte concentration calculation. *J. Anal. Atomic Spectrom.* 11, 899–904. doi: 10.1039/JA9961100899

Magee, R., Ubide, T., and Kahl, M. (in press). The lead-up to Mount Etna's most destructive historic eruption (1669). Cryptic recharge recorded in clinopyroxene. *J. Petrol.*

McNutt, S. R. (2005). Volcanic seismology. *Annu. Rev. Earth. Planet. Sci.* 33, 461–491. doi: 10.1146/annurev.earth.33.092203.122459

Métrich, N., Bertagnini, A., and Di Muro, A. (2010). Conditions of magma storage, degassing and ascent at stromboli: new insights into the volcano plumbing system with inferences on the eruptive dynamics. *J. Petrol.* 51, 603–626. doi: 10.1093/petrology/egp083

Métrich, N., and Clocchiatti, R. (1996). Sufur abundance and its speciation in oxidized alkaline melts. *Geochim. Cosmochim. Acta* 60, 4151–4160. doi: 10.1016/S0016-7037(96)00229-3

Mollo, S., Blundy, J., Scarlato, P., De Cristaofaro, S. P., Tecchiato, V., Di Stefano, F., et al. (2018). An integrated P-T-H_2O-lattice strain model to quantify the role of clinopyroxene fractionation on REE+Y and HFSE patterns of mafic alkaline magmas: application to eruptions at Mt. Etna. *Earth Sci. Rev.* 185, 32–56. doi: 10.1016/j.earscirev.2018.05.014

Mollo, S., Blundy, J. D., Iezzi, G., Scarlato, P., and Langone, A. (2013). The partitioning of trace elements between clinopyroxene and trachybasaltic

melt during rapid cooling and crystal growth. *Contrib. Mineral. Petrol.* 166, 1633–1654. doi: 10.1007/s00410-013-0946-6

Mollo, S., Del Gaudio, P., Ventura, G., Iezzi, G., and Scarlato, P. (2010). Dependence of clinopyroxene composition on cooling rate in basaltic magmas: implications for thermobarometry. *Lithos* 118, 302–312. doi: 10.1016/j.lithos.2010.05.006

Mollo, S., Giacomoni, P. P., Andronico, D., and Scarlato, P. (2015). Clinopyroxene and titanomagnetite cation redistributions at Mt. Etna volcano (Sicily, Italy): footprints of the final solidification history of lava fountains and lava flows. *Chem. Geol.* 406, 45–54. doi: 10.1016/j.chemgeo.2015.04.017

Mollo, S., and Hammer, J. (2017). Dynamic crystallization in magmas. *EMU Notes Mineral.* 16, 373–418. doi: 10.1180/EMU-notes.16.12

Mollo, S., Lanzafame, G., Masotta, M., Iezzi, G., Ferlito, C., and Scarlato, P. (2011). Cooling history of a dike as revealed by mineral chemistry: a case study from Mt. Etna volcano. *Chem. Geol.* 283, 261–273. doi: 10.1016/j.chemgeo.2011.06.016

Mollo, S., and Masotta, M. (2014). Optimizing pre-eruptive temperature estimates in thermally and chemically zoned magma chambers. *Chem. Geol.* 368, 97–103. doi: 10.1016/j.chemgeo.2014.01.007

Morelli, C., Giese, P., Cassinis, R., Colombi, B., Guerra, I., Luongo, G., et al. (1975). Crustal structure of southern Italy. A seismic refraction profile between Puglia-Calabria-Sicily, *Boll. Geofis. Teor. Appl.* 17, 183–210.

Nimis, P. (1995). A clinopyroxene geobarometer for basaltic systems based on crystals-structure modeling. *Contrib. Mineral. Petrol.* 121, 115–125. doi: 10.1007/s004100050093

Orlando, A., D'Orazio, M., Armienti, P., and Borrini, D. (2008). Experimental determination of plagioclase and clinopyroxene crystal growth rates in an anhydrous trachybasalt from Mt. Etna (Italy). *Eur. J. Mineral.* 20, 653–664. doi: 10.1127/0935-1221/2008/0020-1841

Panza, G. F., Peccerillo, A., Aoudia, A., and Farina, B. (2007). Geophysical and petrological modelling of the structure and composition of the crust and upper mantle in complex geodynamic settings: the Tyrrhenian sea and surroundings. *Earth Sci. Rev.* 80, 1–46. doi: 10.1016/j.earscirev.2006.08.004

Paton, C., Hellstrom, J., Paul, B., Woodhead, J., and Hergt, J. (2011). Iolite: freeware for the visualisation and processing of mass spectrometric data. *J. Anal. Atomic Spectrom.* 26, 2508–2518. doi: 10.1039/c1ja10172b

Peccerillo, A. (2005). *Plio-Quaternary Volcanism in Italy*. Berlin: Springer-Verlag.

Perinelli, C., Mollo, S., Gaeta, M., Pia de Cristofaro, S., Palladino, D. M., Armienti, P., et al. (2016). An improved clinopyroxene-based hygrometer for Etnean magmas and implications for eruption triggering mechanisms. *Am. Mineral.* 101, 2774–2777. doi: 10.2138/am-2016-5916

Petrone, C. M., Braschi, E., Francalanci, L., Casalini, M., and Tommasini, S. (2018). Rapid mixing and short storage timescales in the magma dynamics of a steady-state volcano. *Earth Planet. Sci. Lett.* 492, 206–221. doi: 10.1016/j.epsl.2018.03.055

Petrus, J. A., Chew, D. M., Leybourne, M. I., and Kamber, B. S. (2017). A new approach to laser-ablation inductively-coupled-plasma mass spectrometry (LA-ICP-MS) using the flexible map interrogation tool 'Monocle'. *Chem. Geol.* 463, 76–93. doi: 10.1016/j.chemgeo.2017.04.027

Pino, N. A., Moretti, R., Allard, P., and Boschi, E. (2011). Seismic precursors of a basaltic paroxysmal explosion track deep gas accumulation and slug upraise. *J. Geophys. Res.* 116:B02312. doi: 10.1029/2009JB000826

Putirka, K. D. (2008). Thermometers and barometers for volcanic systems. *Rev. Mineral. Geochem.* 69, 61–120. doi: 10.2138/rmg.2008.69.3

Putirka, K. D. (2017). Down the crater: where magmas are stored and why they erupt. *Elements* 13, 11–16. doi: 10.2113/gselements.13.1.11

Putirka, K. D., Johnson, M., Kinzler, R. J., Longhi, J., and Walker, D. (1996). Thermobarometry of mafic igneous rocks based on clinopyroxene-liquid equilibria, 0–30 kbar. *Contrib. Mineral. Petrol.* 123, 92–108. doi: 10.1007/s004100050145

Putirka, K. D., Mikaelian, H., Ryerson, F., and Shaw, H. F. (2003). New clinopyroxene-liquid thermobarometers for mafic, evolved, and volatile-bearing lava compositions, with applications to lavas from Tibet and the Snake River Plain, Idaho. *Am. Mineral.* 88, 1542–1554. doi: 10.2138/am-2003-1017

Reubi, O., and Blundy, J. (2007). A dearth of intermediate melts at subduction zone volcanoes and the petrogenesis of arc andesites. *Nature* 461, 1269–1273. doi: 10.1038/nature08510

Rosi, M., Pistolesi, M., Bertagnini, A., Landi, P., Pompilio, M., and Di Roberto, A. (2013). Stromboli volcano, Aeolian Islands (Italy): present eruptive activity and hazards. *Geol. Soc. Lond. Mem.* 37, 473–490. doi: 10.1144/M37.14

Scarlato, P., Mollo, S., Blundy, J., Iezzi, G., and Tiepolo, M. (2014). The role of natural solidification paths on REE partitioning between clinopyroxene and melt. *Bull. Volcanol.* 76:810. doi: 10.1007/s00445-014-0810-1

Schleicher, J. M., Bergantz, J. W., Breidenthal, R. E., and Burgisser, A. (2016). Time scales of crystal mixing in magma mushes. *Geophys. Res. Lett.* 43. doi: 10.1002/2015GL067372

Shinohara, H. (2008). Excess degassing from volcanoes and its role on eruptive and intrusive activity. *Rev. Geophys.* 46, 1–31. doi: 10.1029/2007RG000244

Spilliaert, N., Allard, P., Métrich, N., and Sobolev, A. V. (2006). Melt inclusion record of the conditions of ascent, degassing, and extrusion of volatile-rich alkali basalt during the powerful 2002 flank eruption of Mount Etna (Italy). *J. Geophys. Res.* 111:B04203. doi: 10.1029/2005JB003934

Streck, M. J. (2008). Mineral textures and zoning as evidence for open system processes. *Rev. Mineral. Geochem.* 69, 595–622. doi: 10.2138/rmg.2008.69.15

Taddeucci, J., Palladino, D. M., Sottili, G., Bernini, D., Andronico, D., and Cristaldi, A. (2013). Linked frequency and intensity of persistentvolcanic activity at Stromboli (Italy). *Geophys. Res. Lett.* 40, 1–5. doi: 10.1002/grl.50652

Ubide, T., Galé, C., Larrea, P., Arranz, E., and Lago, M. (2014). Antecrysts and their effect on rock compositions: the Cretaceous lamprophyre suite in the Catalonian Coastal Ranges (NE Spain). *Lithos* 206–207, 214–233. doi: 10.1016/j.lithos.2014.07.029

Ubide, T., and Kamber, B. (2018). Volcanic crystals as time capsules of eruption history. *Nat. Commun.* 9, 326–326. doi: 10.1038/s41467-017-02274-w

Ubide, T., McKenna, C. A., Chew, D. M., and Kamber, B. S. (2015). High-resolution LA-ICP-MS trace element mapping of igneous minerals: in search of magma histories. *Chem. Geol.* 409, 157–168. doi: 10.1016/j.chemgeo.2015.05.020

Ubide, T., Mollo, S., Zhao, J. X., Nazzari, M., and Scarlato, P. (2019). Sector-zoned clinopyroxene as a recorder of magma history, eruption triggers, and ascent rates. *Geochim. Cosmochim. Acta* 251, 265–283. doi: 10.1016/j.gca.2019.02.021

Villaseca, C., Dorado, O., and Orejana, D. (2019). Mineral chemistry of megacrysts and associated clinopyroxenite enclaves in the Calatrava volcanic field: crystallization processes in mantle magma chambers. *J. Iber. Geol.* 45, 401–426. doi: 10.1007/s41513-019-00101-3

Vona, A., and Romano, C. (2013). The effects of undercooling and deformation rates on the crystallization kinetics of Stromboli and Etna basalts. *Contrib. Mineral. Petrol.* 166, 491–509. doi: 10.1007/s00410-013-0887-0

Welsch, B., Faure, F., Bachèlery, P., and Famin, V. (2009). Microcrysts record transient convection at Piton de la Fournaise Volcano (La Réunion Hotspot). *J. Petrol.* 50, 2287–2305. doi: 10.1093/petrology/egp076

Welsch, B., Hammer, J., Baronnet, A., Jacob, S., Hellebrand, E., and Sinton, J. (2016). Clinopyroxene in postshield Haleakala ankaramite: 2. Texture, compositional zoning and supersaturation in the magma. *Contrib. Mineral. Petrol.* 171:6. doi: 10.1007/s00410-015-1213-9

White, R., and McCausland, W. (2016). Volcano-tectonic earthquakes: A new tool for estimating intrusive volumes and forecasting eruptions. *J. Volcanol. Geotherm. Res.* 309, 139–155. doi: 10.1016/j.jvolgeores.2015.10.020

Conflict of Interest Statement: YB was employed by company TOFWERK AG at the onset of this project.

The remaining authors declare that the research was conducted in the absence of any commercial or financial relationships that could be construed as a potential conflict of interest.

Copyright © 2019 Ubide, Caulfield, Brandt, Bussweiler, Mollo, Di Stefano, Nazzari and Scarlato. This is an open-access article distributed under the terms of the Creative Commons Attribution License (CC BY). The use, distribution or reproduction in other forums is permitted, provided the original author(s) and the copyright owner(s) are credited and that the original publication in this journal is cited, in accordance with accepted academic practice. No use, distribution or reproduction is permitted which does not comply with these terms.